APTw imaging in Paediatric low-grade Gliomas during Treatment at 7T

Relation between APTw images and clinical outcome

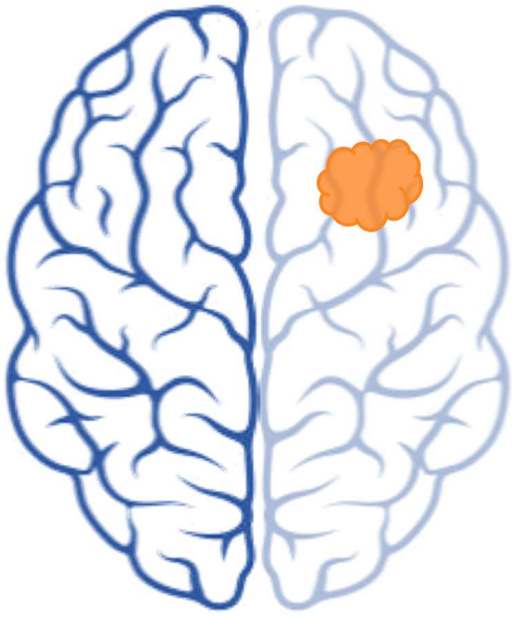

Karleen T. Oonk

April 3, 2024

prinses máxima centrum kinderoncologie

UMC Utrecht

UNIVERSITY OF TWENTE.

APTw imaging in Paediatric low-grade Gliomas during Treatment at 7T

A thesis presented for the degree of Master of Science in Technical Medicine

by

Karleen T. Oonk

April 3, 2024

Graduation committee

Chair:	Prof. Dr. Ir. B. ten Haken[1]
Medical supervisor:	Dr. M.H. Lequin[2]
Technical supervisor:	Dr. Ir. L. Alic[1]
Daily supervisors:	Dr. ir. J.P. Wijnen[2] and Dr. ir. E.C. Wiegers[2]
Process supervisor:	E.M. Walter, MSc[1]
External member:	Dr. A.T.M. Bellos - Grob[1]

1. University of Twente, Faculty of Science and Technology, Drienerlolaan 5, 7522 NB Enschede, the Netherlands
2. University Medical Center Utrecht, Department of Radiology, Heidelberglaan 100, 3584 CX Utrecht, the Netherlands

The study described in this thesis was performed at the Department of Radiology, UMC Utrecht in collaboration with the Princess Máxima Center for Pediatric Oncology, and with technical support from the University of Twente.

UNIVERSITY OF TWENTE.

Preface

One year ago, I started my graduate internship in the High Field group at the Radiology department of the UMC Utrecht. After a search, I ended up at this place where I got the opportunity to combine my interest in paediatric neuro-oncology with the clinical implementation of advanced MR techniques. It was a beautiful year full of learning opportunities, challenges, successes, conviviality, and also difficulties and pitfalls. This thesis presents the results of my graduation project titled *APTw imaging in Paediatric low-grade Gliomas during Treatment at 7T*. With this, I hope to obtain my MSc in Technical Medicine, specialised in *Medical Imaging and Interventions*.

Completing this project would not have been possible without the help and support of many people. First of all, I would like to thank Jannie and Evita. Thank you for the opportunity for me to perform my graduation project at the UMC Utrecht in combination with the Princess Màxima Center. I appreciate your technical and academic knowledge, enthusiasm, and confidence in my abilities. You made me feel comfortable in situations where I felt insecure. You were always approachable for discussion and questions. This made me feel at home in the research group. Additionally, I would like to thank Maarten for the opportunities to get insights into the work of a paediatric radiologist and your clinical view of my project. I want to thank Lejla Alic for her critical view, technical support, and time to meet with me every two weeks. I enjoyed our conversations from a technical perspective while maintaining the clinical question in mind. I also want to thank you for your belief and confidence in my abilities. Furthermore, I would like to express my gratitude to Elise Walter, as my mentor and to Jessie and Nan as peers, for creating an open space to share our ideas and struggles, ask questions, and have a laugh. Without their help, I would not have developed into the professional I am today.

I also want to thank all other colleagues from the UMC Utrecht and Princess Màxima Center who participated in my research. Sabine, thank you for helping me include patients in the MITCH study and for sharing your expertise on paediatric brain tumours during the outpatient clinic. Hans, thank you for your technical knowledge to help me create a method for B_1 inhomogeneity correction at 7T. Giorgio, thank you for sharing your knowledge in ophthalmology and opportunities to learn about visual function testing in paediatric patients. Lastly, Emiel and Wouter for allowing me to continue my clinical development in radiology while Maarten was away. Moreover, I want to thank the students from the High Field research group for our great times during our precious coffee and lunch breaks, drinks at the Basket and Orloff, and our little game sessions. Thank you all for these memorable moments. Also, I want to show my gratitude to Bernhard ten Haken for his positive mindset en words as chair of my graduation committee, and Anique Bellos-Grob for taking part in this committee.

Finally, I want to thank my family, housemates, and close friends for their never-ending support during my study and graduation project. You are the best!

Karleen Oonk
Utrecht, April 2024

Abstract

Introduction: Paediatric low-grade gliomas, the most common central nervous system (CNS) tumours in children, often require adjuvant chemotherapy or radiation therapy due to incomplete surgical removal. MR imaging may not reliably reflect tumour behaviour, posing challenges in monitoring treatment effects (e.g., pseudoprogression). Improving the diagnosis and evaluation of treatment effectiveness for paediatric brain tumours could be enhanced through non-invasive characterization of tumour metabolism. Amide proton transfer weighted (APTw) imaging holds promise as a potential imaging biomarker for treatment response. However, current applications of APTw imaging primarily focus on adult brain tumours not allowing direct translation to the paediatric population.
Objectives: To generate APTw maps, acquired at 7T, to assess treatment effects over time in paediatric patients with low-grade brain tumours. In addition, a method to correct for B_1 inhomogeneity is investigated by creating a patient-specific ratio map of the chemical exchange saturation transfer (CEST) effect in the brain.
Material and methods: APTw images belonging to the phantom and thirteen paediatric patients were acquired at 7T. Depending on the acquisition protocol, normalised and B0-corrected z-spectra were processed pixel-wise by MTRasym and/or Lorentzian fitting to obtain APTw maps. The phantom contained five submerged falcon tubes with solutions of Nicotinamide (50 mM). A ratio map was created of the CEST effect in the phantom, which corrected the APTw maps for B_1 inhomogeneity. The variance in APTw values in the corrected and uncorrected maps was evaluated by calculating the mean and standard deviation. In 13 paediatric patients changes of the APTw values inside the tumour at different time points were assessed and compared to healthy brain tissue and the clinical outcome (responsive, stable or progressive) of the patients. Additionally, in five patients the method for B_1 correction was applied.
Results: A reduction in APTw variance was observed following the application of B1 correction to the data obtained from a homogeneous phantom. Furthermore, APTw maps, quantified with both Lorentzian fitting as MTR asymmetry, of thirteen paediatric brain tumours were obtained. In the APTw maps, quantified with Lorentzian fitting, the tumour was indistinguishable from normal brain tissue. On the other hand, in the APTw maps, quantified with MTRasym, the tumour was distinguishable. The APTw values, quantified with MTRasy, were significantly higher in LGG compared with normal brain tissue at all time points ($p_{baseline} = 0.0032$, $p_{followup1} = <0.001$, and $p_{followup2} = 0.001$).
Conclusion: The phantom study indicates that with a simulated ratio map of the CEST effect, which represented the B1 inhomogeneity, more homogeneous APTw maps can be created. Furthermore, APTw maps, quantified with both Lorentzian fitting as MTR asymmetry, of thirteen paediatric brain tumours, did not have any relation with the clinical outcome of these patients both in the uncorrected and corrected data. However, in the APTw maps, quantified with MTR asymmetry, the average APTw value of the tumours was significantly higher than the average APTw value in normal brain tissue. APTw imaging at 7T for assessing treatment outcomes in paediatric LGG is not yet robust enough, due to movement, too little SNR, and B_1 inhomogeneity.
Keywords: APTw imaging, MRI, paediatric brain tumours, B_1 inhomogeneity, clinical outcome.

Contents

List of Abbreviations

^{31}P MRSI	Phosphorus magnetic resonance spectroscopy imaging
APT	Amide proton transfer
APTw	Amide proton transfer weighted
B	Baseline
B_0	Static magnetic field
B_1	Radiofrequency pulse amplitude
BCVA	Best corrected visual acuity
CEST	Chemical exchange saturation transfer
CNS	Central nervous system
DLGNT	Diffuse leptomenigeal glioneuronal tumour
DREAM	Dual refocusing echo acquisition mode
DS	Direct water saturation
DWI	Diffusing weighted imaging
FLAIR	fluid-attenuated inversion recovery
FOV	Field of view
FU1	Follow up 1
fU2	Follow up 2
FWHM	Full width half maximum
GCL	Ganglion cell layer
HGG	High grade glioma
IPL	Inner plexiform layer
LF	Lorentzian fitting
LGG	Low grade glioma
MDO	Multidisciplinairy board
METC	Medical ethical committee
MITCH	Metabolic imaging of tumours in children
MRI	Magnetic resonance imaging
MT	Magnetization transfer
MTR_{asym}	Magnetization transfer ratio asymmetry
NA	Nicotinamide
NMR	Nuclear magnetic resonance
NOE	Nuclear overhauser effect
OCT	Optical coherence tomography
OPG	Optic pathway glioma
PMC	Princess Màxima Center for Paediatric Oncology
ppm	Parts per million
RAPNO	Response assessment in paediatric neuro oncology
RF	Radiofrequency
RNFL	Retinal nerve fibre layer
ROI	Region of interest
S_0	Unsaturated z-spectral point
SAR	Specific absorption rate
SEGA	Subependymal giant cell astrocytoma
SNR	Signal-to-noise ratio
S_{sat}	Saturated z-spectral point
STEAM	Stimulated echo Aacquisition mode
TE	Echo time
TR	Repetition time
WASABI	Simultaneous mapping of the water shift and B_1

List of Figures

List of Tables

1 Introduction

1.1 Paediatric brain tumours

In the Netherlands about 120 children per year are diagnosed with a brain or spinal cord tumour, making central nervous system (CNS) tumours the second most common form of paediatric cancer after leukaemia.[2] A child with a brain tumour can show a wide spectrum of symptoms. The most common symptoms in children with a brain tumour are headaches, nausea and vomiting, abnormalities of gait and coordination, papilledema, and seizures. These symptoms are largely determined by the location of the tumour.[3] Magnetic Resonance Imaging (MRI) is used to determine the localisation, size, and extension of the tumour. A standard brain MRI protocol consists of pre- and post-contrast T1-weighted, T2-weighted, fluid-attenuated inversion recovery (FLAIR), and diffusion-weighted (DW) sequences. To determine the tumour type histopathology is necessary. Depending on risk stratification and diagnosis (high-grade glioma (HGG) or low-grade glioma (LGG)) or tumour type, treatment options include neurosurgery, (chemo)radiation therapy, and/or chemotherapy. Resection of the tumour is often the first step in the treatment after radiological diagnosis. The goal of neurosurgery is to remove as much tumour tissue as possible while maintaining functional integrity.[4] However in some children the risk of damaging important structures is high and (complete) tumour resection is challenging. For these children, adjuvant chemo- and/or radiation therapy is considered as treatment of choice.[5]

1.2 Treatment monitoring

To evaluate therapeutic response, children with a brain tumour are monitored every three to six months during treatment through neurological exams, ophthalmic exams, and conventional MRI. After treatment, the time between follow-up exams is extended to a maximum of one year. Depending on the tumour type the total follow-up period can vary from five to ten years. New or worsened symptoms indicate an earlier check-up.

1.2.1 Physical and neurological exam

The physical and neurological examinations are performed by an oncologist and neurologist to test the nervous system and include looking at the patient's vision, hearing, alertness, muscle strength, coordination, and reflexes. The vision is tested by looking at the movement of the eye and questioning the patient about double vision. The hearing is evaluated using an otoscope by looking at the ear canal and eardrum and by asking the patient and caregiver about the hearing. The neurologist will also talk to the patient and caregiver to evaluate the patient's alertness, speech, and responses. The muscle strength and balance are tested by having the patient push with his/her arms and legs against the hand of the neurologist. In addition, the patient has to walk from one point to another over a straight line. Lastly, the reflexes of the patient are tested with the use of a reflex hammer.[6]

1.2.2 Ophthalmic exam

Children with a brain tumour in or near the optic pathway are also monitored by an ophthalmologist. An ophthalmic exam consists of an orthoptic evaluation, best-corrected visual acuity (BCVA), pupillary responses, slitlamp examination, visual field examination, and ophthalmoscopy. Orthoptic evaluation comprises ocular motility and convergence, stereopsis, refraction, light reflex, and cover tests, as well as patient inspection and observation. Age-appropriate testing techniques (e.g. with pictures and interrupted circles) are used to examine the BCVA monocularly. Slitlamp examination assesses the eye's anterior portion. To evaluate the existence and degree of optic disc edema and optic nerve atrophy, ophthalmoscopy is used. The visual field examination in younger patients is evaluated by the behavioural visual field screening test, in which children have to respond to a ball on a graded arc that moves from behind to the centre of the visual field from different angles.[7, 8] In older patients the visual field examination is done by the peritest, in which patients have to respond to a light in a large hemisphere that lights up.[9]
Another technique that is used to evaluate the visual function of the patient is optical coherence tomography (OCT). It is a non-invasive, in vivo, imaging modality which uses low-coherence interferometry to provide high-resolution images of ocular tissue. On the OCT images, it is possible to distinguish multiple retinal layers around the optic nerve head and the macula. Especially the retinal nerve fiber layer (RNFL) and the ganglion cell layer-inner plexiform layer (GCL-IPL) thickness (Figure 1.1) have the potential to be a good measurement for the detection of visual function and visual field loss in children with a brain tumour, particularly in visual pathway tumours.[10]

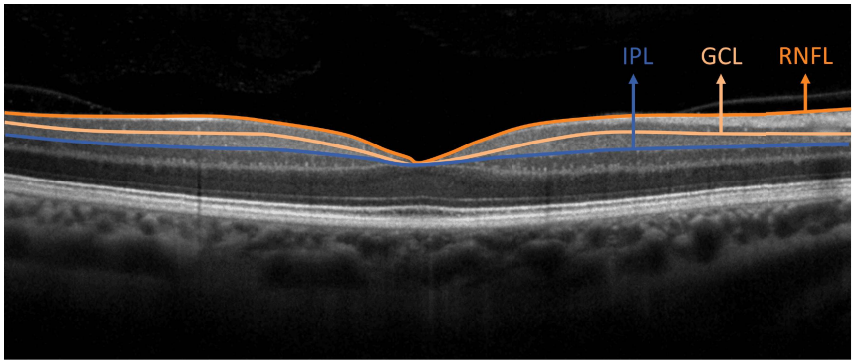

Figure 1.1: OCT image of macular retinal layers. In orange the retinal nerve fiber layer, in light orange the ganglion cell layer, and in blue the inner plexiform layer.

1.2.3 Conventional MRI

The conventional MRI scans (pre- and post-contrast T1-weighted, T2-weighted, FLAIR, and diffusion-weighted sequences) are made every three to six months during follow-up and are assessed by a radiologist. The Response Assessment in Paediatric Neuro-oncology (RAPNO) guideline (Panel 1) is used clinically to evaluate the behaviour of the paediatric brain tumour.[11, 12] However, the difference between tumour progression and pseudoprogression (progression related to treatment effect) cannot always be determined with certainty on conventional MRI.[13]

- **Complete response** is a complete disappearance of the target lesion and all areas of metastatic disease on T2-weighted and T2-weighted fluid-attenuated inversion recovery imaging and contrast imaging using the baseline MRI or best-recorded response for comparison.
- **Major response** is a 75% or greater reduction in the target lesion but insufficient response to qualify as a complete response (both an increase and a decrease in enhancement do not contribute overall).
- **Partial response** is a 50% or greater reduction in the target lesion, typically on T2-weighted and T2-weighted-fluid-attenuated inversion recovery imaging, and variable changes in enhancement (both an increase and a decrease in enhancement do not contribute overall) using the baseline MRI for comparison.
- **Minor response** is a 25%-49% reduction in the target lesion, usually assessed by T2-weighted and T2-weighted fluid-attenuated inversion recovery imaging (both an increase and a decrease in enhancement do not contribute overall) using the baseline MRI for comparison.
- **Stable disease** is an increase or a decrease in the target lesion that is not sufficient to qualify as a progressive disease or responsive disease.
- **Progressive disease** A greater than 25% increase in the target lesion, usually assessed on T2-weighted and T2-weighted fluid-attenuated inversion recovery imaging (both an increase and a decrease in enhancement do not contribute overall), or the development or substantial growth (>25%) of new or metastatic lesions using the baseline MRI or best-recorded response for comparison.

Panel 1: RAPNO response criteria for assessment of paediatric low-grade gliomas.[11]

1.2.4 Multidisciplinary board

The multidisciplinary board is responsible for discussing and combining all the results of the individual exams (e.g., neurological exam, ophthalmic exam, and radiological exam). The board consists of all of the neurologists and oncologists, and a radiologist, ophthalmologist, and pathologist. Together, they assess, based on the individual exams, how the tumour responds to the treatment and determine when it is necessary to alter or begin the course of treatment as well as when the patient completed the treatment.

1.3 APTw imaging

Advanced MRI sequences can contribute to the non-invasive characterisation of paediatric brain tumour metabolism. One of these MR techniques is amide proton transfer weighted (APTw) imaging, which provides information about peptide levels in the tissue through an indirect measure of the reduction of the water signal.[14] APTw maps and the histopathological cell proliferation marker Ki-67 show a strong correlation. As a result, APTw maps appear to be a promising imaging biomarker for the behaviour of the tumour at the metabolic level.[15, 16]
APTw imaging shows potential for diagnostic applications in neuro-oncology, particularly to distinguish between high- and low-grade gliomas.[15, 16, 17, 18] Furthermore, in high-grade gliomas, APTw imaging has also been observed to distinguish between pseudoprogression and tumour progression.[13] In addition, APTw imaging is suggested as a possible imaging biomarker for evaluating the efficacy of treatment for brain tumours. However, all these studies are performed on adult brain tumours which

are different from paediatric brain tumours concerning their clinical, biological, and radiological characteristics. There are limited studies that use APTw imaging. An example is a study which uses APTw imaging as a biomarker for H3 K27 alteration of paediatric brainstem gliomas.[19] Another study, which uses APTw imaging in paediatric neuro-oncology shows that paediatric brain tumours, low-grade and high-grade, could be characterised. However, this research included a small number of patients (23 patients).[20] Therefore, more research is needed before the current APTw maps application can be translated to the paediatric population and their suitability should be carefully evaluated.

1.4 Aim of the study

A non-invasive method to assess tumour activity is needed and APTw maps emerge as a promising imaging biomarker for assessing tumour behaviour at the metabolic level. Therefore, this study aims to generate APTw maps, acquired at 7T, to assess treatment effects over time in paediatric patients with low-grade brain tumours.

2 | Technical background

2.1 General principle of APTw imaging

Amide proton transfer-weighted (APTw) imaging is a non-invasive MR technique based on chemical exchange saturation transfer (CEST) that provides information about peptide and proton levels in tissue. CEST is an MR imaging contrast approach in which exogenous or endogenous compounds are detected through an indirect detection of the reduction of the water signal.[21] This reduction is a result of a difference in resonance frequency for different molecules, known as chemical shift. This change in resonance frequency is caused by varying levels of electron shielding of protons of different solutes. A higher electron shielding results in a lower resonance frequency. Radiofrequency (RF) irradiation is used to selectively saturate exchangeable solute protons that resonate at a frequency slightly different from water using the chemical shift principle.[21] The saturated molecules are in a temporary state, with an equal number of spins against the magnetic field to those aligned with the magnetic field, showing no net magnetization. The saturated protons are then exchanged with unsaturated protons from the bulk water. As a result of this exchange, the water signal is attenuated. One single transfer of saturation is not sufficient to show any noticeable influence on water protons. However, the water pool is far bigger than the saturated solute proton pool. Therefore, each transferring saturated solute proton is replaced by an unsaturated water proton, which is again saturated. The saturation time must be long enough for the saturated protons in the bulk water to accumulate. As a result, low concentrations of solutes become indirectly visible.[14, 21] Figure 2.1 depicts the principle of CEST.

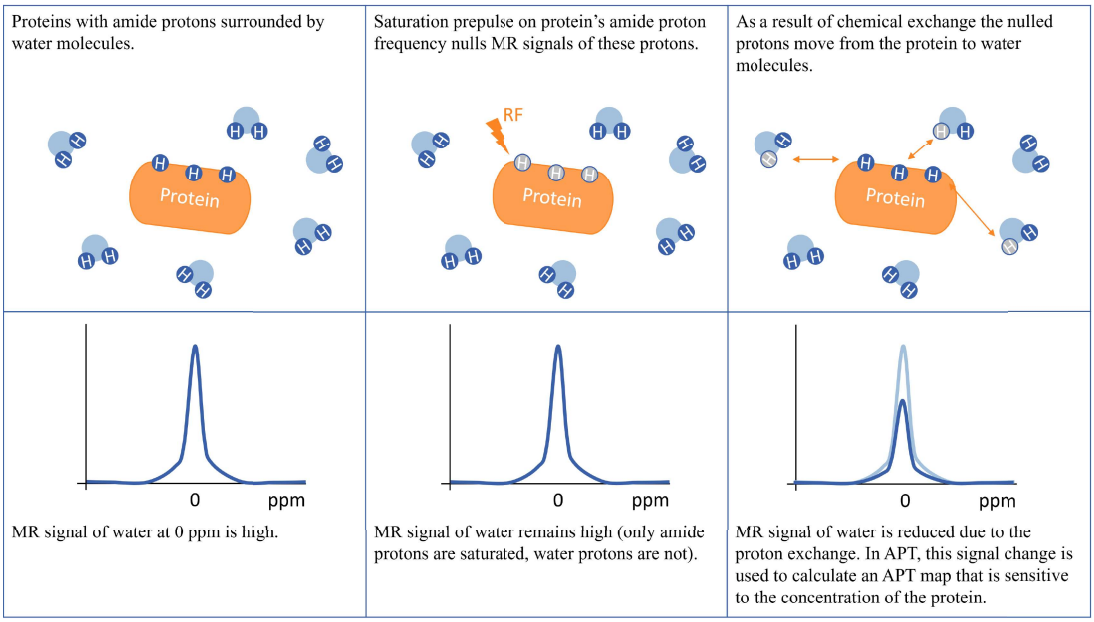

Figure 2.1: A visual representation of the general principle of CEST. The bottom row shows the effect of the saturation and magnetization transfer on the proton spectrum.[1]

This mechanism continues to lower the water magnetization while the saturation pulse is applied. T_1 relaxation restores the saturated protons to their normal state until the system reaches a steady state or the saturation pulse is turned off.[22] It is important to have a slow exchange process for CEST imaging to be successful. To distinguish between the two groups, the exchange rate (k_{ex}) between the chemical substance and water must be less than the chemical shift.[14]

2.2 Acquisition of APTw images

To increase the water signal reduction, CEST acquisition requires a continuous long RF pulse (in order of seconds; Figure 2.2a) to exchange sufficient saturated protons. However, the long RF pulse requires a lot of power, which causes hardware problems (heating of the amplifier), and increases the specific absorption rate (SAR). An increase in SAR causes heating of tissue, which can be harmful to the patient. Therefore, an alternative pulsed saturation can be used, in which protons are saturated and exchanged within each pulse. The interpulse gap allows the tissue to heat up less but increases the total scan time.[14] In children, it is preferred to keep the scan time as short as possible. Therefore, pulsed saturation with alternation between the even and odd channels is used. This reduces the SAR effects and the total scan time concerning the other two saturation options.[23, 24]

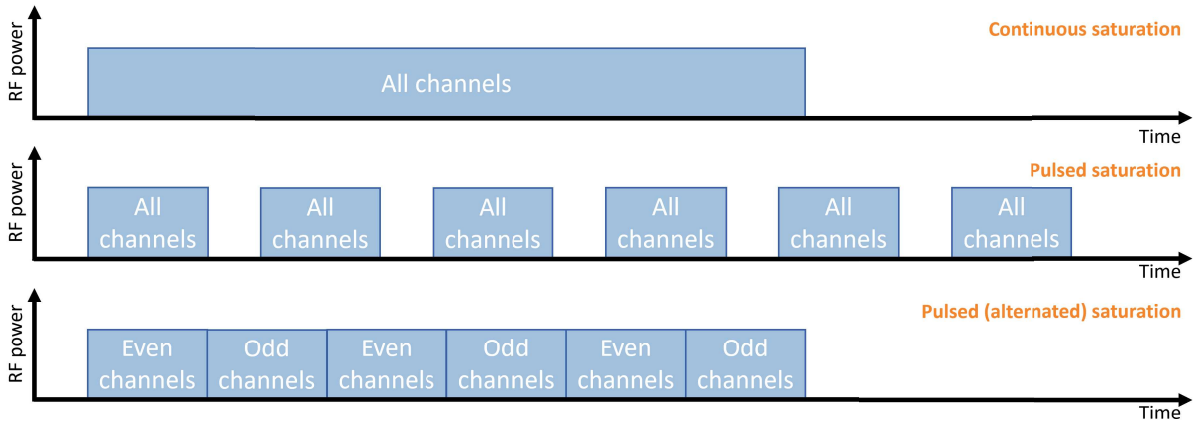

Figure 2.2: Schematic illustration of the different saturation schemes; continuous saturation, pulsed saturation, and pulsed (alternated) saturation.

2.3 Z-spectrum

The z-spectrum is a plot of the water attenuation against the off-resonance saturation frequency. This spectrum is created by dividing the unsaturated water signal by the saturated water signal (see Figure 2.3). The water resonance frequency, shown in Figure 2.3a and 2.3b at 4.75 ppm, is the symmetry axis of the z-spectrum, thus is therefore assigned to zero ppm in CEST imaging, see Figure 2.3c. The other resonance frequencies are scaled concerning the water frequency, e.g. the resonance frequency of amides is around 3.5 ppm.

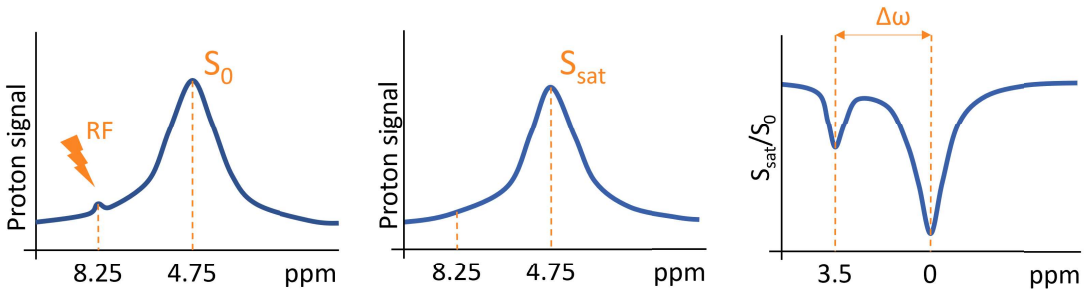

(a) (b) (c)

Figure 2.3: (a) and (b) Solute protons are saturated at their specific resonance frequency and this saturation is then transferred to water. (c) The z-spectrum in which the measurement of normalised water saturation is seen.

2.4 Quantification metric

CEST quantification metrics are used to quantify endogenous contrast, i.e. create APTw maps. To quantify the APT-CEST signal, conflicting effects such as direct water saturation (DS) and the magnetization transfer effect (MT) must be eliminated. MT is caused by the magnetization transfer of non-saturated water protons and saturated protons of semisolid macromolecules. DS is caused by a direct saturation of the water by the RF pulse. These effects, MT and DS, can be eliminated by using post-processing quantification methods like magnetic transfer ratio asymmetry (MTRasym) and Lorentzian fitting (LF).[14]

2.4.1 MTRasym

MTRasym is based on the symmetry around the water frequency (0 ppm). It compares the water signal reduction on opposite spectral positions (+$\Delta\omega$ and -$\Delta\omega$ concerning water).[14, 21] The MTR_{asym} can be calculated using Formula 2.1.

$$MTR_{asym}(+\Delta\omega) = \frac{S_{-\Delta\omega} - S_{+\Delta\omega}}{S_0} \tag{2.1}$$

$S_{+\Delta\omega}$ and $S_{-\Delta\omega}$ are the measured water signals after saturation with a specific RF pulse at $+\Delta\omega$ and $-\Delta\omega$. The MTR_{asym} for APTw imaging is performed at +3.5ppm because this is the chemical shift of amides.[14] However, other effects like the nuclear overhauser enhancement (NOE) and semisolid macromolecular magnetization transfer (MT) may interfere with MTR_{asym}.[25]

2.4.2 Lorentzian fitting

The quantification metric Lorentzian fitting uses the sum of different Lorentzian functions to fit the z-spectrum. Previous knowledge of the amplitude, full width half maximum (FWHM), and frequency offset for various endogenous contrasts form the basis of the Lorentizan functions. The Levenberg-Marquardt algorithm is used to fit the parameters.[26, 27] The function used for Lorentzian fitting is shown in Formula 2.2.

$$L_i(\Delta\omega) = A_i \frac{\frac{\Gamma_i^2}{4}}{\frac{\Gamma_i^2}{4} + (\Delta\omega - \delta i)^2} \tag{2.2}$$

Γ_i is the Lorentzian function corresponding to the offset frequency $\Delta\omega$. The amplitude A_i, full width half maximum Γ_i, and the frequency shift from the free water proton δi are considered.[28] Lorentzian fitting can also measure other parameters than APT. A 5-pool Lorentzian fitting the following parameters are quantified: APT (3.5 ppm), NOE (-3.5 ppm), direct saturation (DS), MT, and amines

(2.2 ppm). The NOE effect is caused by a shift in transition through dipolar or magnetic coupling of nearby nuclei.[25]

2.5 APTw imaging at 7T

APTw imaging, in this study, is done at a 7T system, which provided compared to a lower field strength, enhanced signal-to-noise (SNR), contrast, and higher resolution of the images. In addition to these benefits, the chemical shift increases at a higher magnetic field strength. This is beneficial because the exchange rate needs to be smaller than the chemical shift.[14] A higher chemical shift allows us to quantify other effects, such as NOE, DS, MT, and amines.[29] Another benefit is that at 7T, water has a longer T1 relaxation time, which makes it possible for the water pool to become more saturated, and this raises the detectable CEST effect.[14]

However, by using a higher magnetic field strength the inhomogeneities of the static magnetic field (B_0) and radiofrequency transmit field (B_1) are also increased, which causes artifacts (see Figure 2.4). B_0 inhomogeneity is caused by variations in tissue magnetic susceptibility. The B_0 inhomogeneity artifacts, including geometric distortion, signal dropout, and blurring, are particularly strong at places where air and tissue interface, such as the frontal sinus and ear canals.[30] B_1 inhomogeneity is caused by shorter RF wavelengths due to a higher Larmor frequency of the protons[31, 32] and the attenuation of RF amplitude due to tissue conductivity[33, 34]. Shorter wavelengths generate RF pulse interference because they propagate more slowly and have higher tissue resistive losses. To compensate for B_0 and B_1 inhomogeneity, post-processing techniques are needed.

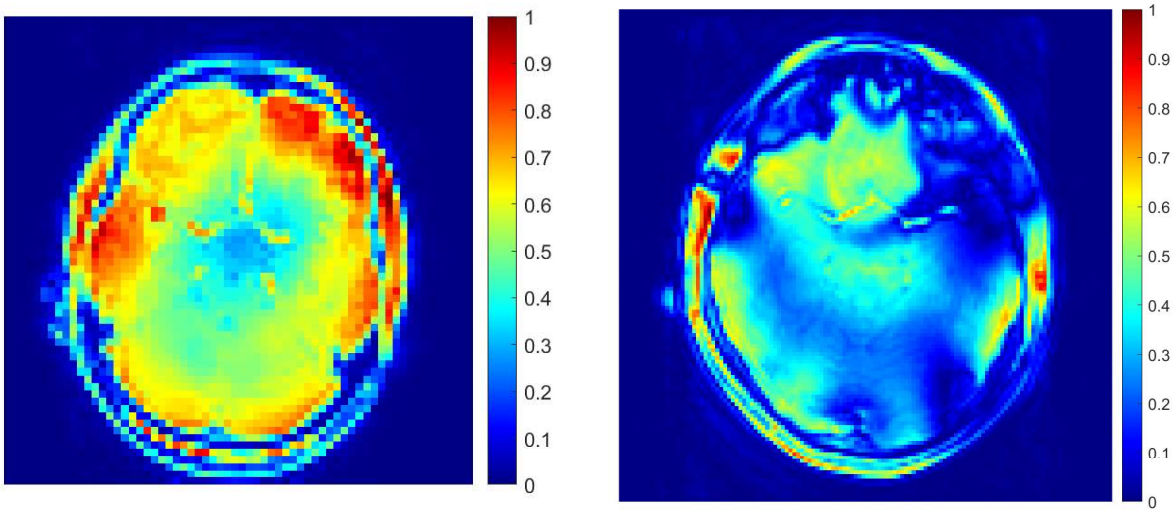

(a) B_0 map

(b) B_1 map

Figure 2.4: Examples of acquired B_0 and B_1 maps in which the inhomogeneity in the brain is visible.

3 | Phantom study

3.1 Introduction

All APTw images of the patients in this study were acquired with a 7T system. However, by using a higher magnetic field strength the inhomogeneity of the B_0 and B_1 field is also increased. These inhomogeneities result in artifacts in the acquired images, see section 2.5. The 7T scanner contains a shim coil with 2nd order shimming to decrease static B_0 variations roughly. In addition, a post-processing method is used to fine-tune the B_0 correction. Nonetheless, a method to correct for B_1 inhomogeneity is not yet used. A method to correct for B_1 inhomogeneity is to acquire B_1 maps, which can show the relative inhomogeneity between voxels. There are various methods to acquire these maps, for example, simultaneous mapping of the water shift and B_1 (WASABI)[35], and dual refocusing echo acquisition mode (DREAM)[36]. WASABI is based on the saturation achieved by applying off-resonance irradiation for several frequency offsets around the Larmor frequency of water. The signal can be analysed per voxel to estimate the relative B_0 and B_1 value.[35] DREAM B_1 mapping is based on the single-shot STEAM sequence (see Figure 3.1).[36]

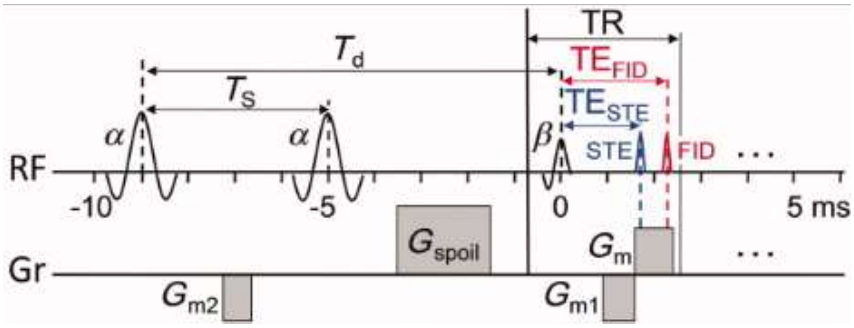

Figure 3.1: Schematic visualisation of the STEAM preparation pulse

Since there is no method to acquire one B_1 map with alternating channels, like how CEST images were acquired described in 2.2, the B_1 maps for the even and odd channels were acquired separately using DREAM. When acquiring these separate B_1 maps, the even and odd channels are not interfering, However, this is the case in CEST. To acquire B_1 maps mimicking the pulse scheme of the CEST sequence a patient-specific simulated B_1 map of the even and odd channels combined is needed. In this phantom study, we first simulated the expected CEST signal to create a patient-specific ratio map of the CEST effect in the brain. With this, we aim to correct the CEST data, of the patients, for B_1 inhomogeneity.

3.2 Method

3.2.1 Phantom characteristics

The phantom is a thermos flask filled with 6 grams salt dissolved in 2L water of 37°C, containing five falcon tubes consisting of the same amide concentrations (Nicotinamide 50 mM). Amides contain a

nitrogen atom connected to a carbonyl. The chemical shift of this molecule is ∼3.5 ppm concerning water.[15] The amide solutes are solved in phosphate-buffered saline (pH ∼7.4). The pH influences the measured APTw value and therefore the fluids in the tubes are titrated to a pH range of ∼7.0 (brain pH) with sodium azide.[37] The pH was measured after each added drop of sodium azide with pH indicator strips till the strip indicated the pH was ∼7.0 (range of pH: 6.8-7.2). A picture and schematic drawing of the phantom is shown in Figure 3.2. The pH measurements of the tubes in the phantom were performed at room temperature.

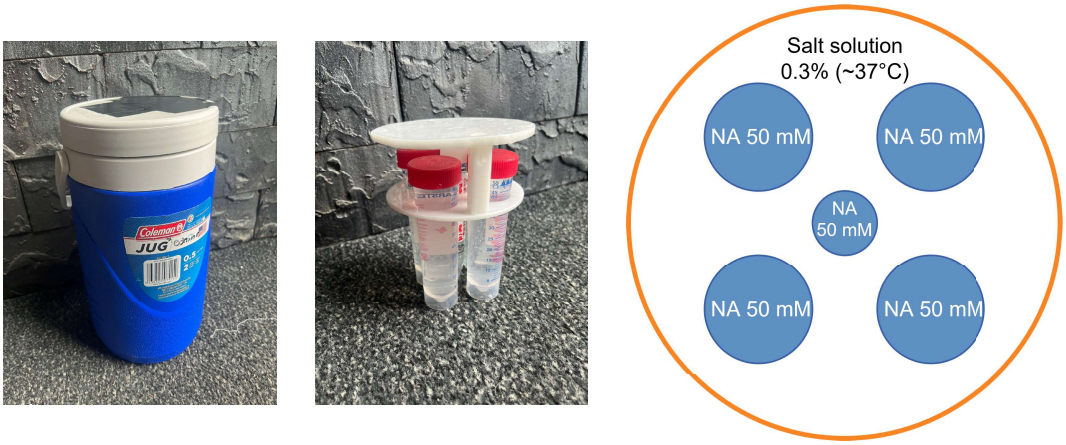

Figure 3.2: (a) Picture of the thermos flask; (b) Picture of the tube arrangement; (c) Schematic drawing of the phantom containing five tubes with all the same concentration of solute amides (Nicotinamide 50 mM). The tubes were surrounded with 0.3% salt solution (∼37°C).

3.2.2 Image acquisition

The APTw maps of the phantom were acquired at a 7T system (Achieva, Philips Healthcare, Best, The Netherlands) using a 32-channel receive-only and 8-channel transmit (8Tx/32Rx) coil for the head (Nova Medical, Wilmington, USA) with a 3D gradient echo sequence. The phantom was diagonally placed in the MRI scanner to remove air bubbles from the field of view. The data was acquired at 33 different frequency offsets between $\Delta\omega = \pm 40$ ppm with dense sampling around the regions of interest ($\Delta\omega$ = -3.5, 0 and 3.5 ppm). The distribution of the offsets was: 0, ±0.20, ±0.27, ±0.50, ±1.17, ±1.84, ±2.60, ±2.80, ±3.00, ±3.20, ±3.34, ±3.65, ±3.80, ±4.20, ±6.71, ±20.00, ±40.00. Two additional offsets at ±600 ppm were added for data normalisation during post-processing. The imaging parameters were TR = 3.75 ms; TE = 1.8 ms; matrix = 128 x 128 x 12; FOV = 256 x 256 x 24 mm; resolution = 2.0 x 2.0 x 2.0 mm; flip angle = 5°. The APTw maps were acquired with an RF pulse amplitude of 1.5 µT. The saturation time equaled 1400 ms (a total of 56 block pulses with a duration of 25 ms).

The B1 maps of the phantom were acquired using the following imaging parameters: TR = 3.7 ms, TE = 1.4 ms, matrix = 112 x 112 x 12, FOV = 224 x 224 x 24 mm, resolution = 2.0 x 2.0 x 2.0 mm, flip angle = 7°. One with only the even transmit channels and one with only the odd channels with the drive scale divided by 0.6, because during the acquisition of the B_1 maps instead of 8 alternating channels only four channels were used. The scaling factor known as the drive scale controlled the applied RF pulse's amplitude and flip angle. The amplitude and flip angle are increased with increasing scaling factor. Simulations have shown that B_1 with half of the channels is 0.6 times lower than with all eight channels.[38].

3.2.3 Image processing

The acquired z-spectra were normalised by dividing the saturated z-spectral (S_{sat}) points by the unsaturated z-spectral (S_0) points ($\Delta\omega$=±600 ppm). The normalised z-spectrum (S_{sat}/S_0) was then

corrected for B_0 inhomogeneity, using MATLAB (R2021a, The MathWorks, Natick: MA), voxel-wise in three steps (see Figure 3.3).

- Identification of the B_0-shift (δ) by detecting the ppm-position of the absolute minimum in the z-spectrum which is the position of the water peak (Figure 3.3A).
- B_0-shift (δ) of the z-spectrum in all the voxels is induced by adjusting the minimum of the normalised signal (water peak) to 0 ppm (Figure 3.3B).
- Interpolation of normalised z-spectrum is applied to achieve a symmetric ppm-distribution (Figure 3.3C).

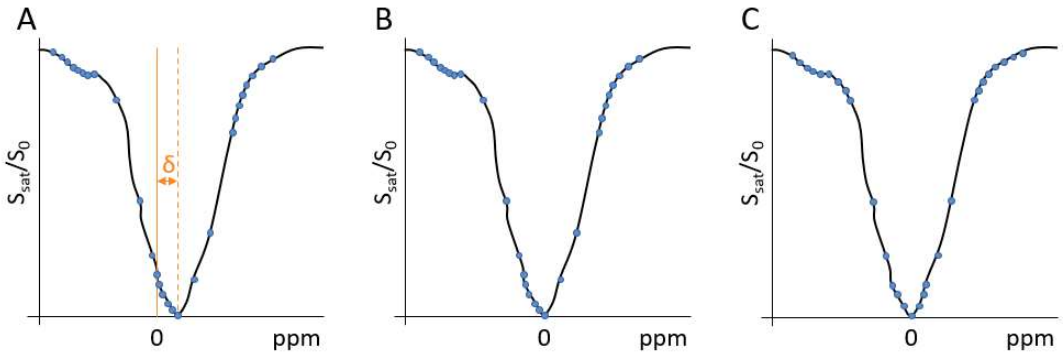

Figure 3.3: The three steps of the B_0 correction. (a) define B_0-shift, (b) shift z-spectrum, and (c) spline interpolation of z-spectral points.

The APTw map was calculated using Lorentzian fitting. Lorentzian fitting incorporates five different pools (DS, MT, NOE, amines, and amides (APT)). The prior knowledge that was used for the Lorentzian fitting is listed in the Appendix A.

3.2.4 Simulation CEST effect

The CEST effect is simulated based on the two-pool model of the Bloch equations. The Bloch equations describe the evolution of magnetisation ($\frac{dM}{dt}$) in the presence of an applied magnetic field (B_0^+).[39] The chemical properties of a CEST agent and various nuclear magnetic resonance (NMR) parameters can be related to the measured CEST effect by the Bloch equations.[40] In Appendix B the Bloch equations (Equation B.1-B.8) for a two-pool model are described, where pool A is bulk water and pool B is amides. The MR behavior of these pools in each direction ($\frac{dMx}{dt}$,$\frac{dMy}{dt}$ and $\frac{dMz}{dt}$) can be described with these equations.[40]

The expected CEST signal is calculated for each saturation pulse (56 pulses). The nominal B_1 that is used for this simulation is 1.5 µT[41] and the input of the simulation was the acquired B1 maps (odd and even) with a DS divided by 0.6. At each saturation pulse of 25 ms, the B_1 maps used as input are alternated. After each pulse, the spins are not fully recovered yet, so for that reason, this simulation used the end position of the spins as the start position for the following saturation pulse of 25 ms. The sum of all the signals from each pulse is the total amount of simulated CEST effect for one offset. This signal is normalised with the mean in the whole phantom and this results in a ratio map of the expected CEST effect. The ratio map, at the offset of amides (3.5ppm), is divided by the APTw maps to obtain the corrected APTw maps.

3.2.5 Data analysis

The APTw values, for both the uncorrected and the, for B_1 inhomogeneity, corrected APTw maps, were evaluated using four data bins. The first bin is filled with voxels outside the tubes and the other three bins were based on the APTw values of the uncorrected APTw maps, see Table 3.1.

	APT values
Bin 1	voxels outside the tubes
Bin 2	greater than or equal to 5% and less than 10%
Bin 3	greater than or equal to 10% and less than 15%
Bin 4	greater than or equal to 15%

Table 3.1: Four bins in which the APT values were evaluated.

Thereafter the variance in the z-spectral points, for each tube and all the tubes together, were evaluated for the uncorrected and the, for B_1 inhomogeneity, corrected APTw maps. The variance of the APTw values was assessed by calculating the mean and standard deviation of each tube and all the tubes together.

3.3 Results

3.3.1 Simulated CEST effect

In Figure 3.4 the simulated CEST effect for offsets 17 to 33 is displayed. The CEST effect is clearly visible between offsets 22 and 31, which are between 1.2 ppm and 4.2 ppm. The CEST effect has the highest value in offset 28 and the second highest value in offset 29, which are at 3.35ppm and 3.65ppm.

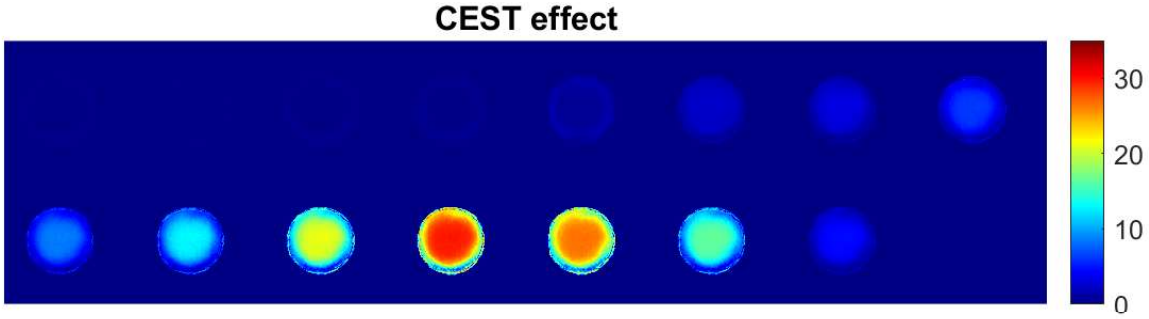

Figure 3.4: Simulated CEST effect displayed in offset 17 to 33.

3.3.2 APTw maps

Figure 3.5a shows the uncorrected APTw map of the phantom. Generally, high APTw values, around 15%, are seen in the middle of the phantom, and low APTw values, around 7%, are seen at the edges of the phantom. In Figure 3.5b, the APTw maps corrected for B_1 inhomogeneity are displayed. The higher APTw values in the middle of the phantom are not visible anymore and now have approximately the same values as the APTw values at the edges of the phantom, which is around 7%. The variation of the APTw values in the corrected APTw map in every tube is smaller than in the uncorrected APTw maps.

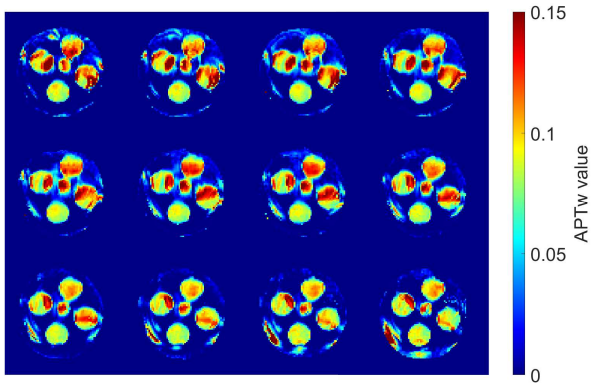

(a) APTw map not corrected for B_1 inhomogeneity.

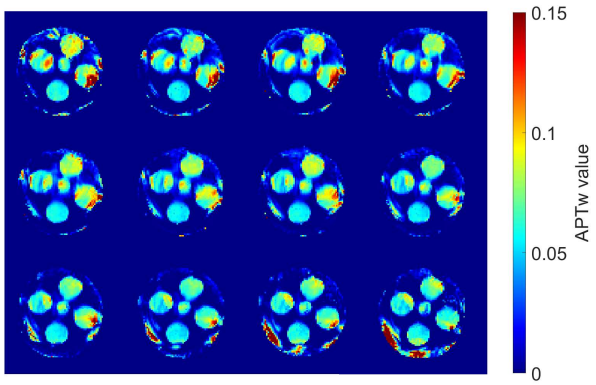

(b) APTw map corrected for B_1 inhomogeneity.

Figure 3.5: The two APTw maps before (a) and after (b) correction for B_1 inhomogeneity.

In Figure 3.6, the uncorrected and corrected data in one slice is seen. In the corrected data (Figure 3.6b), there is a region with a high APTw value in one of the tubes indicated with an arrow. These high values were also seen in the uncorrected data (Figure 3.6a). In Figure 3.6c, the z-spectrum of one voxel in this high APTw value region is shown. It is seen that the original data is noisy and has a splitted water peak. This is not a representable z-spectrum, while the fitted spectrum before and after correction is how a z-spectrum is expected to be.

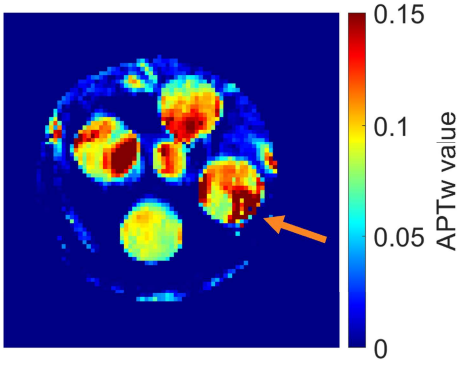

(a) One slice of the uncorrected APTw values in the phantom.

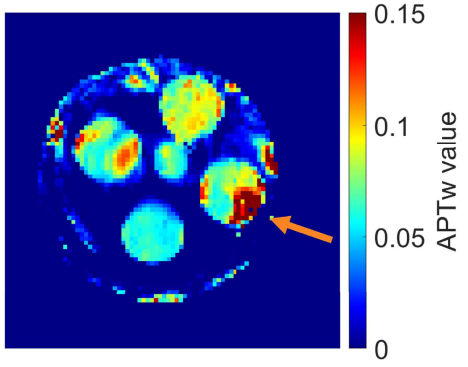

(b) One slice of the corrected APTw values in the phantom.

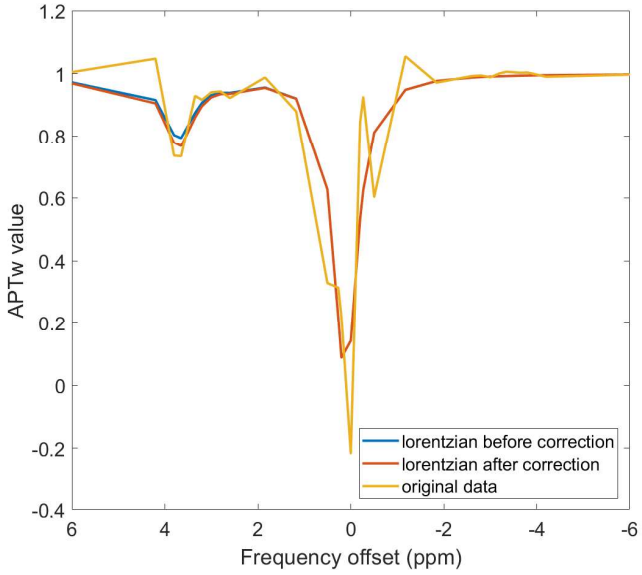

(c) The z-spectrum of the original data (yellow), the fitted data before correction (blue), and the fitted data after correction(red).

Figure 3.6: Some detailed information of the APTw values of the phantom, with (a) uncorrected data; (b) corrected data; (c) z-spectrum of one voxel.

3.3.3 Data

In Figure 3.7 one slice of the voxels in bin 2 (3.7a), bin 3 (3.7b), and bin 4 (3.7c) is shown. Bin 2 contained 4715 voxels, bin 3 contained 3093, and bin 4 contained 421 voxels. The selected voxels in bin 1 were placed outside the tubes, to evaluate the method on voxels where no APT is expected.

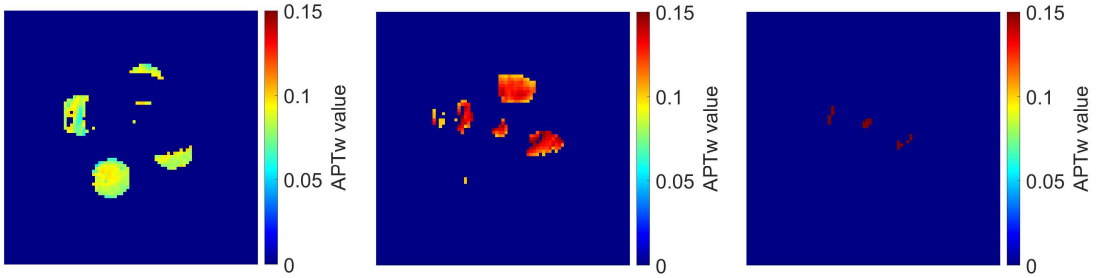

(a) One slice in bin 2 with in total 4715 voxels.

(b) One slice in bin 3 with in total 3093 voxels.

(c) One slice in bin 4 with in total 421 voxels.

Figure 3.7: Visual representation of the voxels in each bin.

In Figure 3.8 the average z-spectrum for each bin is shown, within a) the raw CEST data, b) the fitted z-spectrum, and in c) the corrected fitted z-spectrum. Around 3.5 ppm the APT peak is visible for bins 2, 3, and 4. In these three groups, a difference is seen between the fitted CEST data and the corrected fitted CEST data. The higher the APTw values (bin 4), the greater the drop in de z-spectrum around 3.5 ppm. After correction for B_1, the drop of APT for all three bins is closer to each other. In addition, in bin 1, where no APTw values were measured, there are also no APTw values measured after correction.

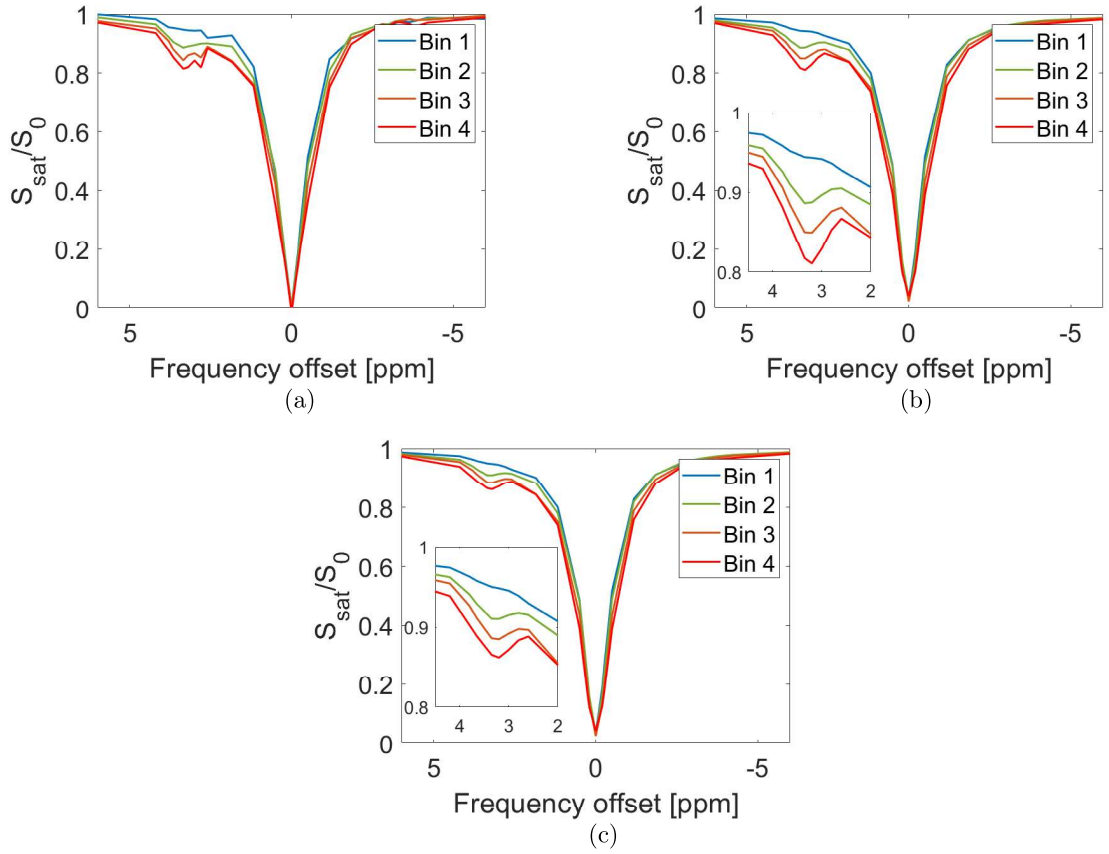

Figure 3.8: The average z-spectrum within (a) the raw CEST data, (b) the fitted CEST data, and (c) the corrected fitted CEST data.

3.3.4 Histogram

In Figure 3.9 a histogram for the APTw values before and after correction is shown. In Figure 3.9a the APTw values of all tubes are shown. It is visible that the distribution of the APTw values before correction is between 5% and 20% with the maximum number of voxels around 8%. After correction, the APTw values are distributed in a smaller range of 4-11% with the maximum number of voxels around 7%. There are also a few outliers visible in the distribution after correction between 15% and 20%.

In Figure 3.9b, 3.9c, 3.9d, 3.9e, and 3.9f the histograms of each tube are shown. The mean APTw value in each tube is decreasing, but also the standard deviation of the APTw values is lower in each tube. This decrease is also seen in Table C.1 in Appendix C, in which the mean and standard deviation for all tubes together and each tube separately are shown. The outliers, with a higher APTw value of 15%-20%, that were described above were visible in tube 3 after correction.

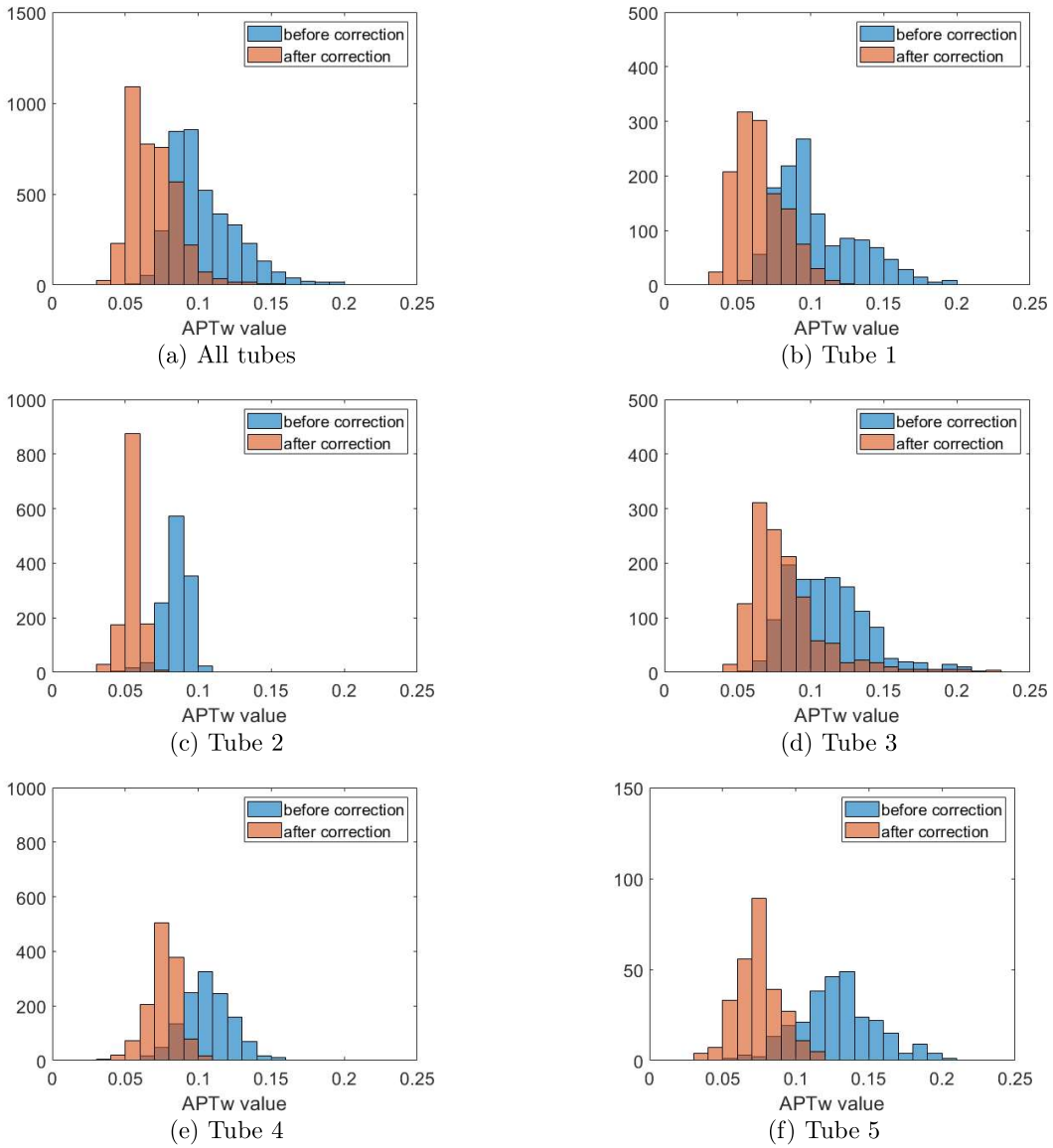

(a) All tubes (b) Tube 1

(c) Tube 2 (d) Tube 3

(e) Tube 4 (f) Tube 5

Figure 3.9: Histograms of the APTw values in all the tubes (Nicotinamide 50 mM) and each tube separately before and after correction.

3.4 Discussion and conclusion

A reduction in APTw variance was observed following the application of B1 correction to the data obtained from a homogeneous phantom. Furthermore, the average APTw values also decreased, which was in line with literature[41]. With a B1 of 1.2µT and a saturation time of 1.4s, it was anticipated that the effect size of amides would approximate 0.6, thereby leading to an expected reduction in the mean APTw value by a factor of 0.6.[41] In addition, in bin 1 low APTw values were seen before correction, because these voxels were outside the tubes in the water. It was shown that the correction method does not create a signal in places where there was no APT present and measured.
The ratio map is normalised with the mean simulated APTw value in the whole phantom. However, it remains unclear whether this average APTw value corresponds to regions lacking B_1 inhomogeneity. However, this does not affect the contrast differences in the phantom. For example, if the APTw value without B_1 inhomogeneity is higher, then the ratio 1 belongs to a higher APTw value.

Lastly, as described before (Section 3.3.4) there are outliers visible in one of the tubes. It is seen that the original data in the red area is not a representable z-spectrum. The outliers, notably prominent in the initial slices of the phantom, may be caused by small air bubbles in the tube persisting within the CEST slab, despite efforts to tilt the phantom. In future work, the z-spectra should have good quality control. Voxels with a spectrum which are not representable, for example when the waterpeak is splitted, should be excluded from the data. One way to assess the quality of the z-spectra is to subtract the fitted z-spectra from the original z-spectra. The expected result is noise from the original data, but when there are multiple peaks or abnormally high peaks the voxel should be excluded from the data. Another option is to add up all the measured z-spectra in the tubes and calculate one mean z-spectrum. This mean z-spectrum can in term be compared with every single z-spectrum. The z-spectrum is excluded if the deviation is above the threshold (mean z-spectrum + standard deviation). An example of this quality assessment method is described in the article of Simpson et al.[42]
A limitation of this study is that the fitting parameters for the Lorentzian fitting were not validated. Validating accurately is challenging due to the inability of phantom measurements to replicate the heterogeneous in-vivo environment that produces confounding effects like MT and NOE.[43] Starting points from published research were used, and grid searches were manually tuned by a previous student until a proper fit was achieved by assessing the fitting's goodness of fit.

4 | Clinical Study

4.1 Introduction

In the clinical study, data from the MITCH (Metabolic Imaging of Tumours in Children) study is used. The MITCH study aims to determine whether APTw imaging and phosphorus magnetic resonance spectroscopy (^{31}P MRSI) at 7T is feasible and suitable for the evaluation of treatment response in paediatric brain tumours. In this thesis, only the APTw imaging of the study was considered; changes in the APTw values inside the tumour at different time points were assessed and compared to the clinical outcome of the patients.

4.2 Method

4.2.1 Study design

The MITCH study was approved by the medical ethical committee (METC Utrecht; Nederlands Trial Register; ID: 8285). Written informed consent was obtained from each patient and/or patient's guardian. Patients underwent three MRI scans at 7T, at baseline, and twice during follow-up examinations in intervals of 3-7 months. The 7T MRI scans were acquired around the same time as the conventional clinical follow-up MRI scans. Between the scans, one group of patients received treatment, which was chemotherapy or radiation therapy. The other group of patients did not receive any treatment and were solely monitored over time (see Figure 4.1).

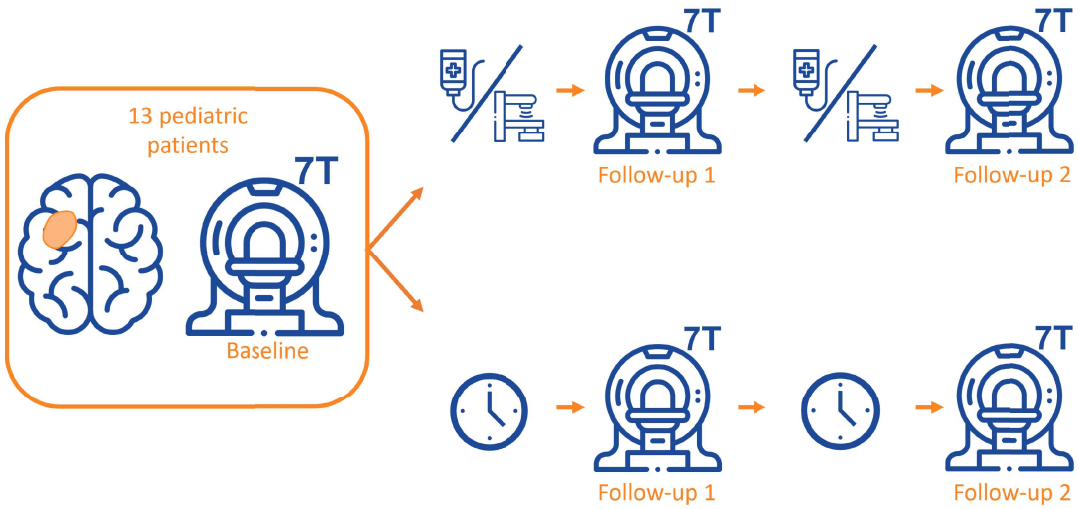

Figure 4.1: The study protocol of the MITCH study.

4.2.2 Patient characteristics

The patients were selected from the Princess Máxima Center for Paediatric Oncology (PMC). Children aged 6 to 18 years diagnosed with a brain tumour, who were capable of undergoing MRI scans without anesthesia, were eligible for inclusion in this study. Patients were on active surveillance or were treated with partial tumour resection, chemotherapy, and/or radiation therapy. Patients were excluded from the study in case of claustrophobia, tumours that were resected within one month, or MRI-specific exclusion criteria, such as metal implants. Each patient was screened for MRI-specific exclusion criteria using the regular MRI (at 7T) safety screening for each MRI scan. For this clinical study, 13 patients were included all with a low-grade glioma (LGG) and each patient had a baseline scan and two MRI sessions during follow-up. The patients participated in the study between January 2021 and February 2024. The patient characteristics of the included patients can be seen in Table 4.1.

	Sex	Age (years)	Diagnosis	Mutation	Treatment
Patient 1	Male	16	Pilocytic astrocytoma	BRAF V600E	Active surveillance
Patient 2	Male	6	Pilocytic astrocytoma	KIAA1549-BRAF	Chemotherapy
Patient 3	Female	16	Optic pathway glioma	Unknown	Chemotherapy
Patient 4	Male	15	Pilocytic astrocytoma	Unknown	Active surveillance
Patient 5	Male	14	Diffuse leptomeningeal glioneuronal tumour (DLGNT)	KIAA1549-BRAF	Chemotherapy
Patient 6	Male	6	Optic pathway glioma	Unknown	Chemotherapy
Patient 7	Male	8	Optic pathway glioma	Unknown	Chemotherapy
Patient 8	Female	9	Optic pathway glioma	Unknown	Chemotherapy
Patient 9	Female	17	Subependymal giant cell astrocytoma (SEGA)	TSC-1/TSC-2	Chemotherapy
Patient 10	Female	6	Optic pathway glioma	Unknown	Chemotherapy
Patient 11	Male	7	Pilocytic astrocytoma	No mutation	Chemotherapy and radiation therapy*
Patient 12	Male	17	Pilocytic astrocytoma	KIAA1549-BRAF	Active surveillance
Patient 13	Male	7	Pilocytic astrocytoma	KIAA1549-BRAF	Chemotherapy

Table 4.1: Patient characteristics of the included patients.
∗Start radiation therapy at follow-up 1

4.2.3 Image acquisition

First FLAIR and T1w anatomical images were obtained with an 8Tx/32Rx head coil (Nova Medical, Wilmington, USA). The acquisition of the APTw images is described in section 3.2.2. The CEST slab in each patient is positioned in a way that contains the entire tumour. In some cases, the slice thickness was doubled to be able to cover the whole tumour (FOV = 256 x 256 x 48 mm, resolution = 2.0 x 2.0 x 4.0 mm). A screenshot of the planning of the CEST slab was made, to ensure comparable orientation of the slab during the follow-up scans. In Figure 4.2 an example of the slab planning for one patient is shown.

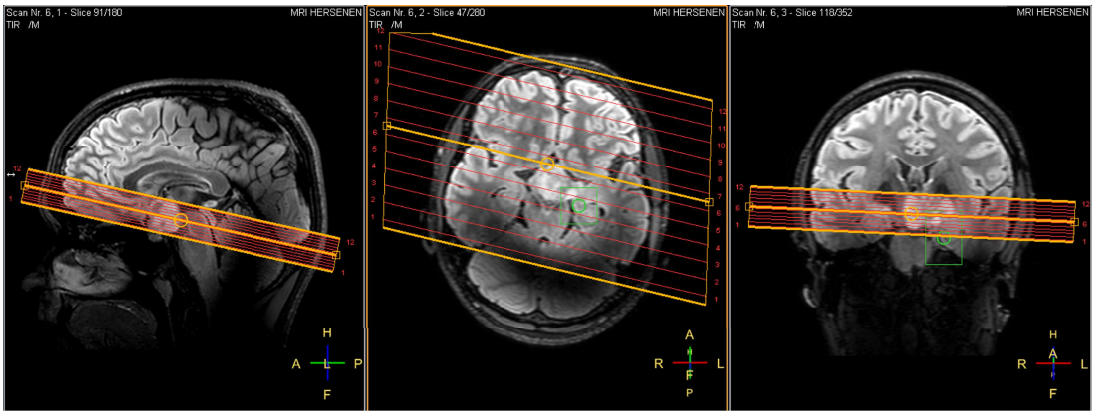

Figure 4.2: Planning of the CEST slab in the brain for APTw image acquisition in three directions (sagittal, transversal, coronal).

4.2.4 Image processing

The z-spectra were normalised and B_0-corrected as described in section 3.2.3. In all patients, the APTw value of each voxel was calculated with MTRasym and Lorentzian fitting. The Lorentzian fitting incorporated five different pools (DS, MT, NOE, amines, and amides (APT)). The prior knowledge that was used for the Lorentzian fitting is listed in Appendix A.[44] Furthermore, for patients with both odd and even B_1 maps available, B_1-correction was performed with a ratio-map as described in Chapter 3. The patients in which B_1-correction was applied are patient 3, 6, 11, 12, and 13. The B_1-correction was only performed with the calculated APTw values with Lorentzian fitting.

4.2.5 Tumour segmentation

The tumours were segmented on FLAIR images and were registered to the CEST coordinate system using linear registration in Elastix. Details of the registration parameters can be found in Appendix D. The performance of the registration was analysed by visual comparison of the registered FLAIR image and unsaturated z-spectral image using ITK-SNAP 3.2.0. In ITK-SNAP also the manual slice-by-slice segmentation of the tumour was performed. All tumour segmentations were confirmed by a neuro-radiologist. See Figure 4.3 for a visual representation of the workflow.

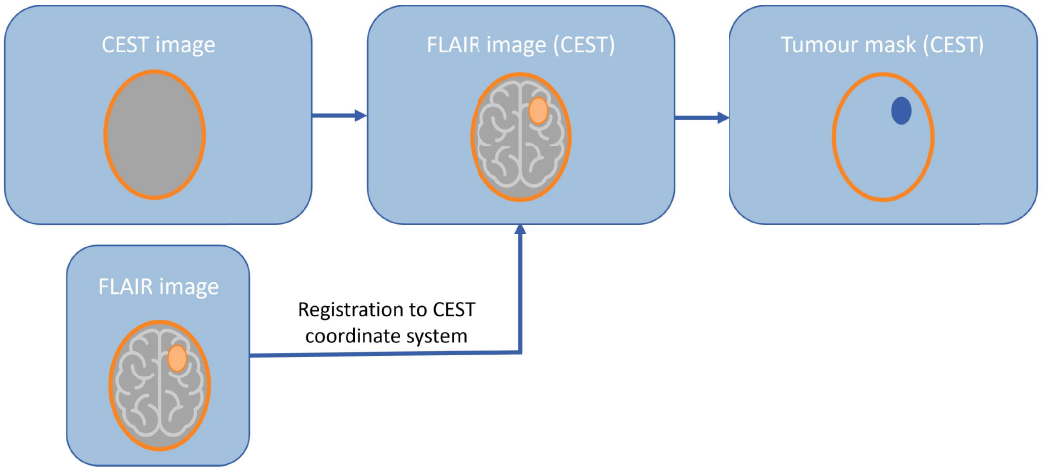

Figure 4.3: Visual representation of the workflow of the registration and tumour segmentation.

4.2.6 Data analysis

The mean APTw values, quantified with Lorentzian fitting and MTRasym, and standard deviation in the tumour for each patient were calculated and the treatment cohort was compared to the active surveillance cohort over time. For patient 3, 6, 11, 12, and 13 the B_1 maps needed as input for the simulation were acquired, and B_1 correction as described in section 3.2.4 was performed. After B_1 correction the APTw values, quantified with Lorentzian fitting, in the tumour were evaluated over time in each patient. In addition, the mean APTw values, quantified with MTRasym, in the tumour were compared to the mean APTw value in the normal brain tissue, and the mean APTw values in pilocytic astrocytomas were compared to other tumour types.

4.2.7 Clinical outcome

The APTw maps were compared to the clinical outcomes of the patients. The clinical outcomes of the patients were categorised into 3 groups: responsive disease, stable disease, and progressive disease. The clinical outcome of each patient between baseline and follow-up 1, between follow-up 1 and follow-up 2, and between baseline and follow-up 2 is determined. This clinical outcome is based on the consensus in the multi-disciplinary board between the oncologists, neurologists, radiologists, pathologists, and ophthalmologists. In addition, the clinical outcome is divided into three subgroups, namely: neurology (i.e., physical and neurological exam), radiology (i.e., RAPNO[11]), and ophthalmology (i.e., vision, visual field, OCT).

4.3 Results

4.3.1 Clinical outcome

In Table 4.2 the clinical outcomes, based on the multidisciplinary board, neurological exams, ophthalmological exams, and radiological exams, of the patients are shown. Based on the multidisciplinary board patient 5 had progressive disease between baseline and follow-up 1, patient 6, 8, and 9 had a responsive disease and the other patients were stable over time. During follow-up 1 to follow-up 2 patient 5, 6, 8, and 11 were progressive and the other patients were stable. Eventually, patient 5 and 11 were stated progressive, and patient 6 en 9 were stated responsive between baseline and follow-up 2. The other patients were deemed stable.

Based on the neurological exams only patient 5 presented with progressive disease. The clinical outcome based on the ophthalmology exams was shown for vision, vision field, and OCT. In some patients, the ophthalmological exams were not available or not reliable. patient 7, 10, and 11 had progressive disease during follow-up. The clinical outcome based on the radiological exams of patient 2, 5, and 11 was progressive disease. In addition, many patients were stable based on RAPNO, while the radiologist still described some growth. The OCT data and tumour dimensions and volumes can be found in Appendix E

		Baseline - Follow-up 1	Follow-up 1 - Follow-up 2	Baseline - Follow-up 2
Patient 1	MDO	🟡	🟡	🟡
	Neurology	🟡	🟡	🟡
	Ophthalmology			
	Vision	🟡	🟡	🟡
	Vision field	🟡	🟡	🟡
	OCT	🟡	🟡	🟡
	Radiology	🟡*	🟡*	🟡*
Patient 2	MDO	🟡	🟡	🟡
	Neurology	🟡	🟡	🟡
	Ophthalmology			
	Vision	🟡	🟡	🟡
	Vision field	🟡	🟡	🟡
	OCT	🟡	🟡	🟡
	Radiology	🔴	🟡	🔴
Patient 3	MDO	🟡	🟡	🟡
	Neurology	🟡	🟡	🟡
	Ophthalmology			
	Vision	🟡	🟡	🟡
	Vision field	🟡	🟡	🟡
	OCT	🟡	🟡	🟡
	Radiology	🟡	🟡	🟡
Patient 4	MDO	🟡	🟡	🟡
	Neurology	🟡	🟡	🟡
	Ophthalmology			
	Vision	🟡	🟡	🟡
	Vision field	🟡	🟡	🟡
	OCT	🟡	🟡	🟡
	Radiology	🟡	🟡	🟡
Patient 5	MDO	🔴	🔴	🔴
	Neurology	🔴	🔴	🔴
	Ophthalmology			
	Vision	-	-	-
	Vision field	-	-	-
	OCT	-	-	-
	Radiology	🟡	🔴	🔴
Patient 6	MDO	🟢	🔴	🟢
	Neurology	🟡	🟡	🟡
	Ophthalmology			
	Vision	-	-	-
	Vision field	-	-	-
	OCT	-	-	-
	Radiology	🟢	🟡*	🟡
Patient 7	MDO	🟡	🟡	🟡
	Neurology	🟡	🟡	🟡
	Ophthalmology			
	Vision	🔴	🟡	🔴
	Vision field	🔴	🟡	🔴
	OCT	🔴	🟡	🔴
	Radiology	🟡	🟡	🟡

Patient 8	MDO	🟢	🔴	🟡
	Neurology	🟡	🟡	🟡
	Ophthalmology			
	Vision	-	🟡	-
	Vision field	-	🔴	-
	OCT	-	-	-
	Radiology	🟡**	🟡*	🟡
Patient 9	MDO	🟢	🟡	🟢
	Neurology	🟡	🟡	🟡
	Ophthalmology			
	Vision	-	-	-
	Vision field	-	-	-
	OCT	-	-	-
	Radiology	🟢	🟡**	🟢
Patient 10	MDO	🟡	🟡	🟡
	Neurology	🟡	🟡	🟡
	Ophthalmology			
	Vision	🔴	🟡	🔴
	Vision field	🔴	🟢	🟡
	OCT	🟡	🟡	🟡
	Radiology	🟡	🟡*	🟡
Patient 11	MDO	🟡	🔴	🔴
	Neurology	🟡	🟡	🟡
	Ophthalmology			
	Vision	🟡	🔴	🔴
	Vision field	🟡	🔴	🔴
	OCT	-	-	-
	Radiology	🟡	🔴	🔴
Patient 12	MDO	🟡	🟡	🟡
	Neurology	🟡	🟡	🟡
	Ophthalmology			
	Vision	-	-	-
	Vision field	-	-	-
	OCT	-	-	-
	Radiology	🟡***	🟡***	🟡***
Patient 13	MDO	🟡	🟡	🟡
	Neurology	🟡	🟡	🟡
	Ophthalmology			
	Vision	🟡	🟡	🟡
	Vision field	🟡	🟡	🟡
	OCT	🟡	🟡	🟡
	Radiology	🟡	🟡	🟡

Table 4.2: The clinical outcome categorised as a responsive disease 🟢, stable disease 🟡, and progressive disease 🔴 based on the consensus in the multi-disciplinary board, the neurological exams, the ophthalmologic exams (vision, vision field, and OCT), and the radiological exams (RAPNO). ∗The radiologist described some growth (a few millimeters).∗∗The radiologist described some reduction (a few millimeters). ∗∗ The radiologist described growth in the cystic component.

4.3.2 APTw maps analysed with Lorentzian fitting

In Figure 4.4 an example of the FLAIR image, tumour mask, APTw maps, and APTw values in the tumour of patient 3 over time can be seen. In this figure, the tumour, located in the lower left just above the ventricle, is indistinguishable. In Appendix F the images of all included patients are depicted. These maps were not corrected for B_1 inhomogeneity. For APT-CEST and the other pools one slice in patient 3 is shown in Figure 4.5. In this figure, at the NOE, DS, and MT slice the tumour, located in the lower left just above the ventricle, can be distinguished.

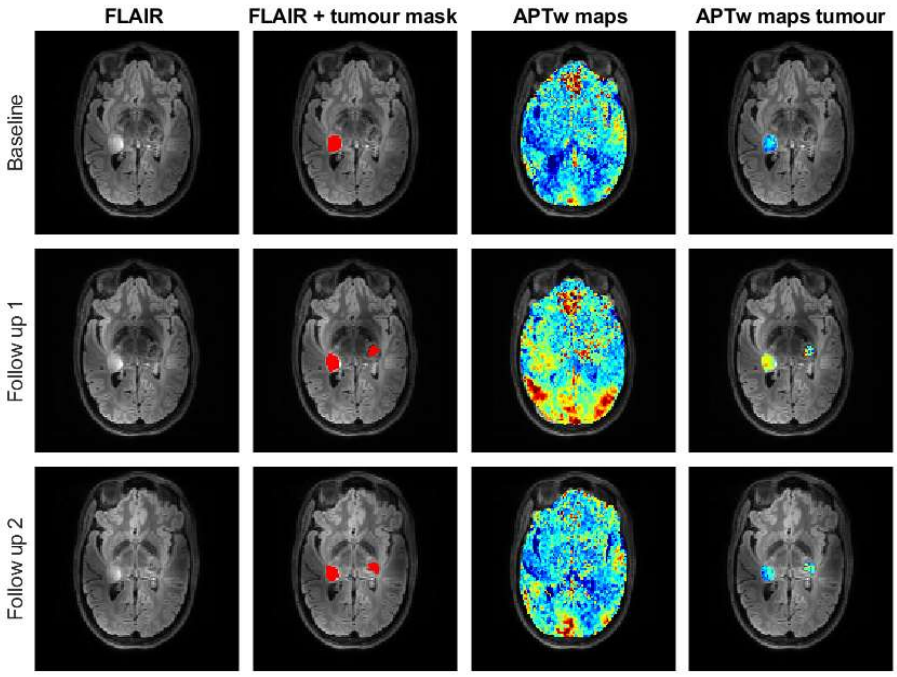

Figure 4.4: Example of the FLAIR image, tumour mask, APTw maps, and APTw values in the tumour of patient 3.

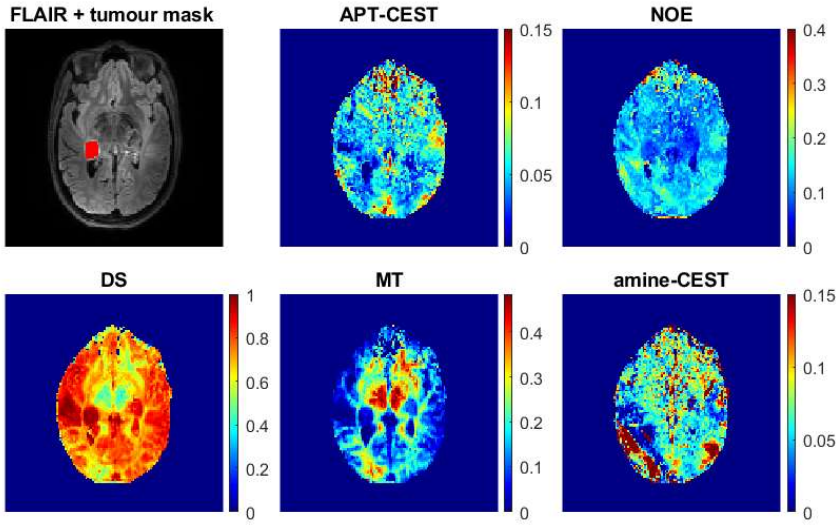

Figure 4.5: One slice of the 5 pools fitted with Lorentzian fitting in patient 3.

In Figure 4.12 the mean APT values in the tumour were compared over time in the treatment and wait-and-scan cohort. The mean value is in both groups around 6-7% and stayed the same during follow-up. Next, in Figure 4.12b the mean APTw value in the tumour of each patient normalised to baseline is shown. In patient, 1, 2, 3, 4, 5, and 10 (only B-FU1) an increase in APTw values during follow-up is shown, while in patient 10 (FU1-FU2) and 13 a decrease in APTw values is shown. The other patients showed a stable APTw value during follow-up.

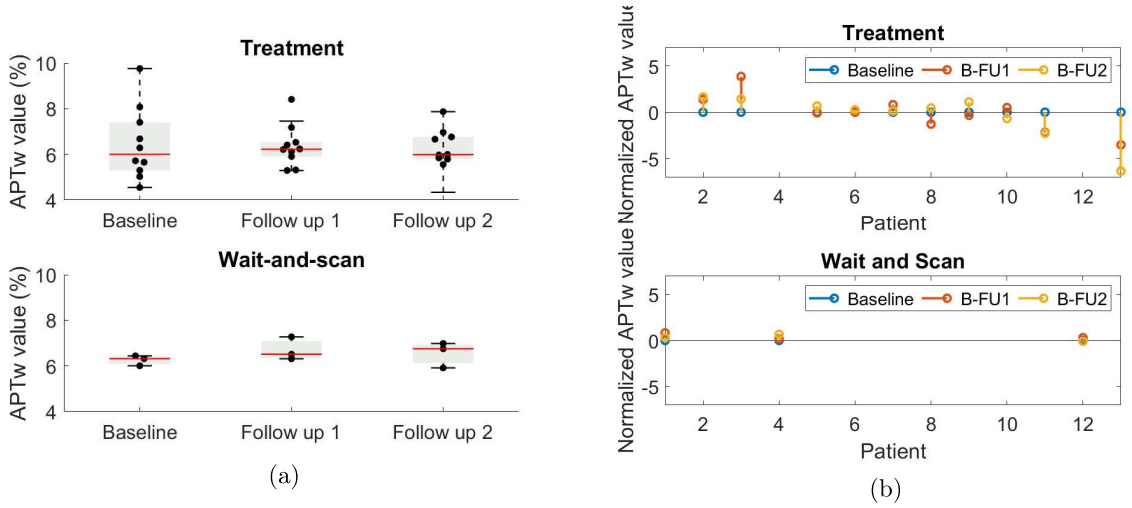

(a) (b)

Figure 4.6: (a) Boxplot of the mean APTw value in the tumour of the treatment and wait-and-scan cohort over time. (b) The mean APTw value in the tumour normalised to baseline over time.

4.3.3 B_1 correction

In Figure 4.7, the uncorrected and corrected APTw map for patient 3 is shown. The APTw values in the corrected APTw map (Figure 4.7b) in the middle of the brain showed a decrease, compared to the uncorrected APTw map (Figure 4.7a). In general, APTw values within the brain appeared more homogeneous, except certain areas along the brain's periphery exhibited higher APTw values.

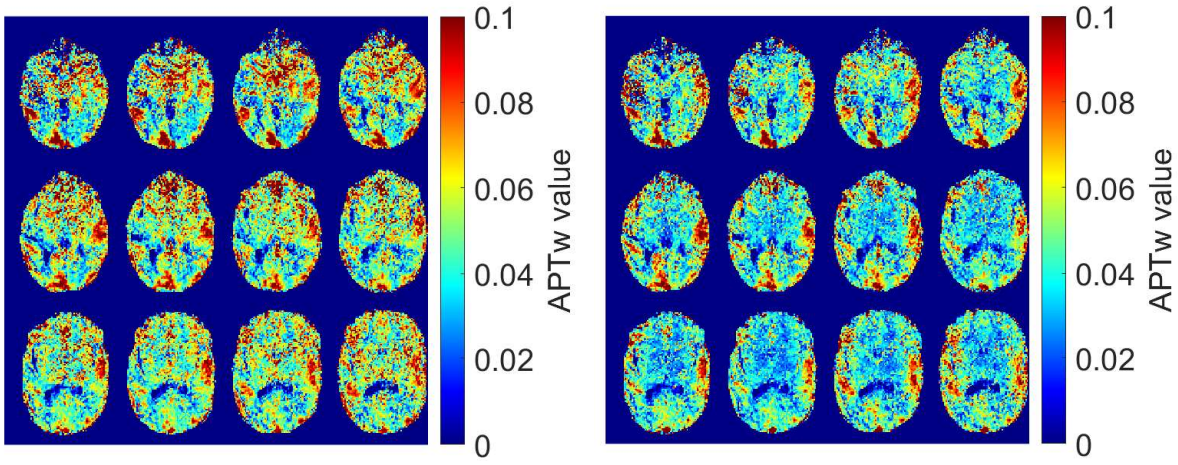

(a) (b)

Figure 4.7: An example of (a) the uncorrected and (b) corrected APTw map of patient 3

In Figure 4.8a the APTw values in the tumour before correction for patient 3, 6, 11, 12, and 13 were

compared with the values after correction. From Figure 4.8 it can be seen that APTw values decreased after correction. In Figure 4.8b is shown that the APTw values after correction in the brain were higher than the values in the tumour.

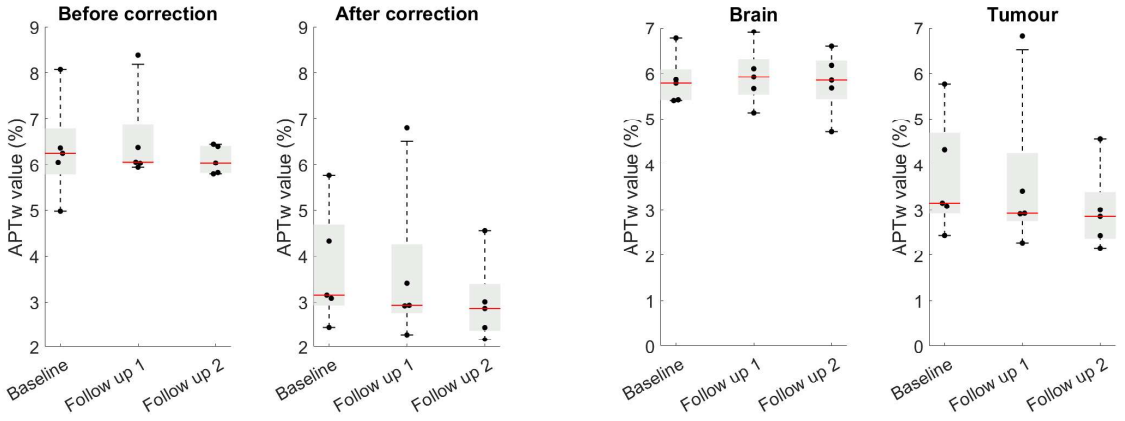

(a) (b)

Figure 4.8: (a) APTw values in the tumour before correction and after correction over time. (b) APTw values after correction in the brain and in the tumour.

In Figure 4.9 the mean APTw values in the tumour of patient 3, 6, 11, 12, and 13 after correction are shown in which the values were normalised to baseline. Between baseline and follow-up 1, patient 3, 6, and 12 show an increase in APTw values, while patient 11 and 13 show a decrease. Between follow-up 1 and follow-up 2, patient 6 shows an increase in APTw values, while patient 3, 11, 12, and 13 show a decrease.

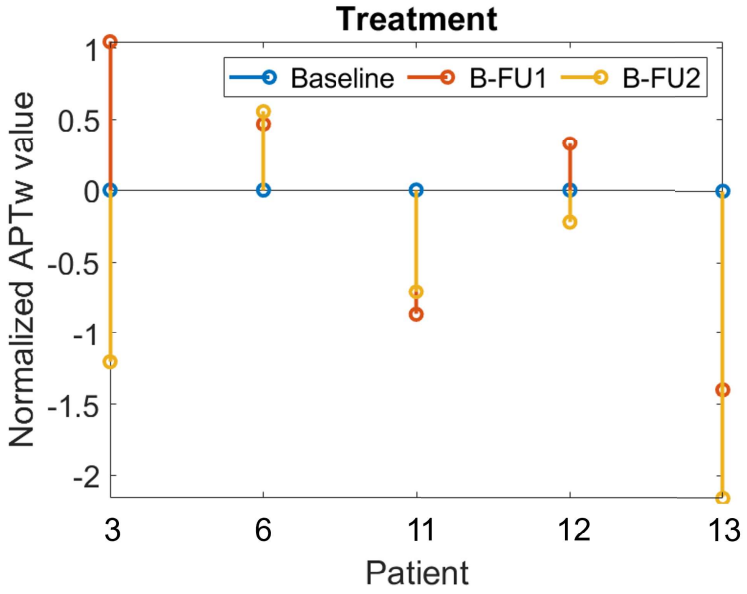

Figure 4.9: Mean APTw value of patient 3, 6, 11, 12, and 13 normalised to baseline.

4.3.4 APTw maps with MTRasymmetry

The APTw values were also quantified using MTRasym. In Figure 4.10 an example of the results for one patient over time is shown. In Appendix G the images of all patients are depicted. In these APTw maps the tumour can be distinguished from the normal brain tissue.

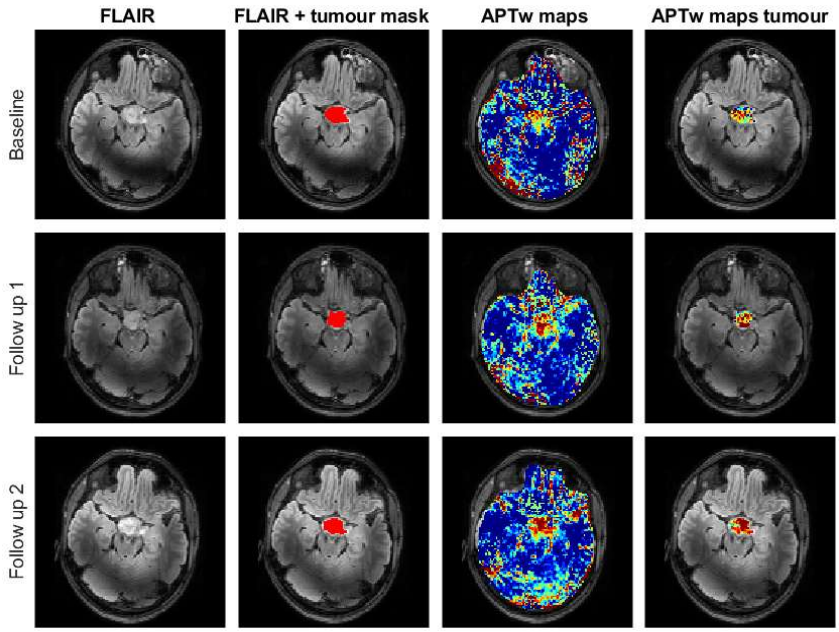

Figure 4.10: An example of the FLAIR, tumour mask, APTw maps quantified with MTRasym and the APTW values in the tumour of patient 1.

In Figure 4.11, the results of comparing the mean APTw values in the tumour with the APTw values in the brain tissue are shown. APTw values are significantly higher in LGG compared with normal brain tissue at all time points (Figure 4.11; $p_{baseline} = 0.0032$, $p_{followup1} = <0.001$, and $p_{followup2} = 0.001$). The mean APTw value was in tumours at baseline 0.61±1.77, at follow up 1 1.06±1.46, and at follow up 2 0.03±3.59. No statistically significant difference is present between the mean APTw value of pilocytic astrocytoma and other types of tumours.

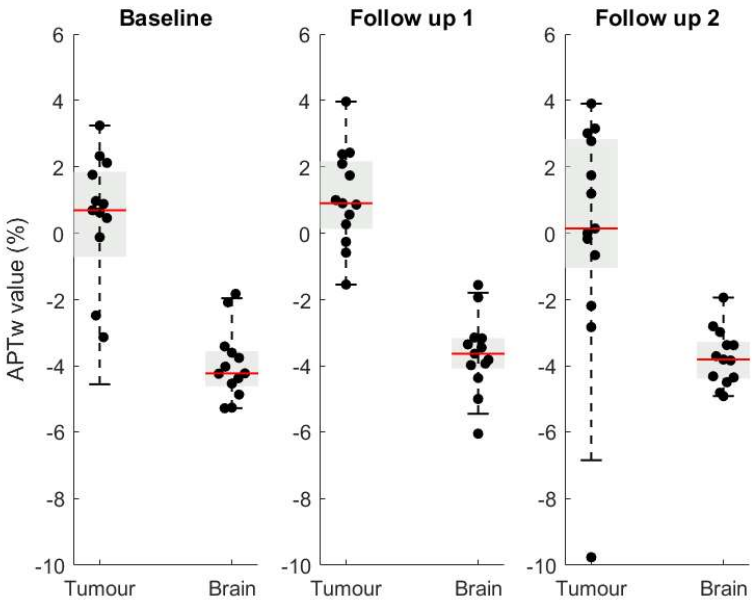

Figure 4.11: Boxplot of the mean APTw values in brain and tumour tissue over time.

In Figure 4.12a the mean APTw values in the tumour were compared over time in the treatment and wait-and-scan cohort. The mean value in both groups is around 0-1% and stayed the same during follow-up. Next, in Figure 4.12b, the mean APTw value in the tumour of each patient normalised to baseline is shown. In patient 1, 2, 3, 7, 9, and 12 an increase in APTw values during follow-up is shown, while in patient 5, 6, 10, and 13 a decrease in APTW values is shown. The other patients showed a stable APTw value during follow-up.

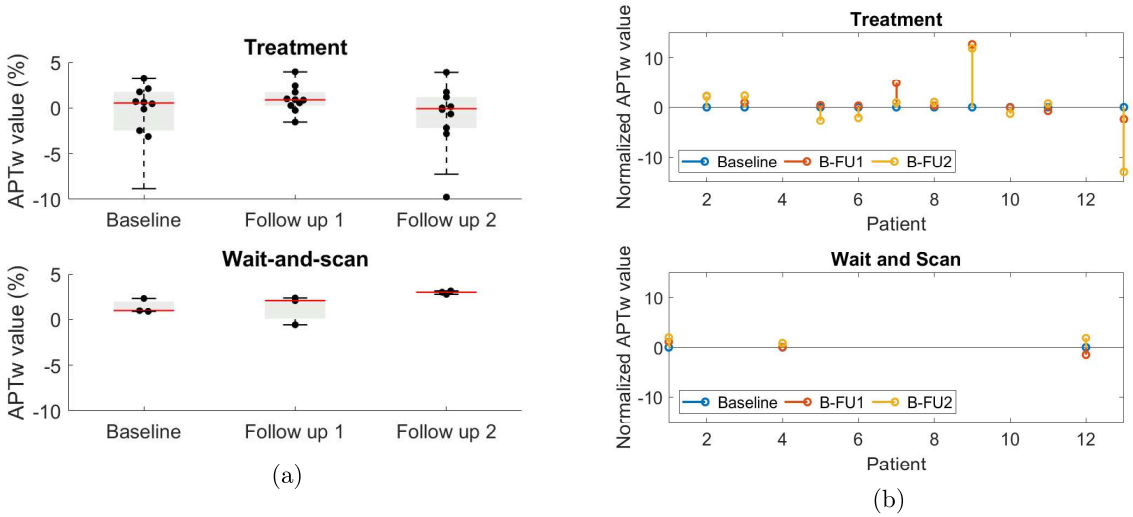

Figure 4.12: (a) The mean APTw value of each patient categorised in the treatment and wait-and-scan cohort over time. (b)The normalised APTw value of each patient over time.

4.4 Discussion and conclusion

The APTw values, quantified with Lorentzian fitting and MTRasym, inside the tumour over time were assessed and related to the clinical outcome of the patients. B_1 inhomogeneity correction, detailed

in Chapter 3, was applied to APTw maps derived from Lorentzian fitting and assessed in relation to clinical outcomes.

4.4.1 Patient cohort

The patient cohort included in this study (thirteen patients) was limited and heterogeneous, with tumours differing in classification, size, and location. Therefore, in most parts, only qualitative analysis was allowed. The limited cohort size resulted in a small wait-and-scan cohort, which consisted of only three patients. More patients in the wait-and-scan cohort should be included when comparing the two groups in the future. In addition, the patients in the treatment cohort (ten patients) had a variety of treatment protocols. Therefore, the effects of treatment on APTw values could not be excluded. An example is the effect of bevacizumab, which could be expected in the treatment of pilocytic astrocytoma (six patients).[45] This type of tumour has enhanced microvascular proliferation. The microvascular proliferation in combination with mobile proteins leaking from this vasculature may result in high APTw values. However, the APTw values may reduce after bevacizumab treatment, because bevacizumab decreases microvascular proliferation.[45, 46]

4.4.2 Clinical outcome

The clinical outcome, based on the MDO, of eight out of thirteen patients was stable during follow-up, and this was also seen in the outcome based on neurological, ophthalmologic, and radiological exams. However, in patient 1 and 12, the radiologist described some tumour growth. In patient 2 this even resulted in progressive disease according to RAPNO. However, the radiologist stated it as pseudoprogression. The patients that had progressive or responsive disease according to the MDO, were also described as progressive or responsive by the radiologist. However, when looking at RAPNO these patients were stated stable. The use of RAPNO for response assessment of LGG could be questioned based on these results. Nevertheless, the RAPNO committee recommends the combined use of imaging, clinical, and functional assessments to evaluate responses in clinical trials. They aim to develop a standardised protocol that can be implemented internationally and prospectively.[11] Future research, should compare the clinical outcome of the neurological, ophthalmologic, and radiological exams over a longer follow-up period. Thereafter, the diagnostic and prospective value of each exam could be investigated, for example, OCT.[47]

4.4.3 Tumour biology

The tumour masks, used to determine the APTw values in the tumour, consisted of only one tumour mask for each patient. These masks included the solid and cystic parts of the tumour. This approach generalised all tumour regions, while elevated levels of mobile proteins are not specific for solid tumour tissue since tumour cysts can contain high protein concentrations as well.[20] Consequently, the average tumour value may not accurately reflect the metabolism of the tumour. In future research, multiple tumour masks should be made to analyse solid and cystic parts separately. In addition, the tumour masks were created on the FLAIR registered to CEST space. However, this resulted in a decrease in resolution, which made tumour segmentation less precise.

4.4.4 APTw maps with Lorentzian fitting

In the APTw maps, quantified with Lorentzian fitting, of all thirteen patients, the APTw values in the tumour were similar to the normal brain making it impossible to distinguish the tumour from the normal brain. This observation contrasts with findings from a study conducted on paediatric LGGs at 3T.[20] There could be multiple reasons for the results in this study. First, it is important to note that the measured APTw values may not solely reflect the presence of proteins and peptides. Instead, the observed APTw contrast originates from the inherent tissue-water T_1 relaxation properties.[48] Additionally, the B_0 and B_1 inhomogeneity are increased at 7T. This study attempted to correct for

these inhomogeneities. However, a gold standard for validating the B_1 correction method remains elusive.
Overall no relation was seen in the mean APTw values in the tumour between the treatment and wait-and-scan group. In addition, the mean APTw values also had no association with the clinical outcome of the patients. Even when the data was corrected for B_1 inhomogeneity, there was no relation found.

4.4.5 APTw maps with MTRasym

The APTw values, quantified with MTRasym, in tumours were statistically higher compared with the APTw values in brain tissue. This may be explained with Figure 4.5 in which the other pools of Lorentzian fitting can be seen. The amides were measured at 3.5 ppm on the z-spectrum. If MTRasym is used 3.5 ppm will be compared to -3.5 ppm, which is the location of the NOE effect. The NOE effect is higher at 7T, and the tumour has a low value in Figure 4.5. This low value in the NOE pool is then visible as a high value in de APTw maps quantified with MTRasym. The low value in NOE signals is in line with literature, where NOE signals are lower than normal brain tissue and also significantly differ between HGG and LGG.[49]. Lastly, there was no relation in the mean APTw values, quantified with MTRasym, between the treatment and wait-and-scan group and between the mean APTw values and the clinical outcome.

4.4.6 Limitation of the clinical study

Two limitations described in Chapter 3 also apply in this chapter, namely the fitting parameters for Lorentzian fitting that were not validated and validation of the B_1 correction method. Furthermore, movement artifacts will be present in young children[50], resulting in inappropriate APTw maps. Therefore, registration of z-spectral images should be taken into consideration in the paediatric population. Additionally, APTw values in healthy brain tissue decrease with age, which makes age a significant covariate to take into consideration, especially for the paediatric population.[20] The influence of age was not investigated due to a limited number of patients. Lastly, APTw values could be affected by the tumour location, for example in areas with large B_0 inhomogeneities like the oral cavity. In this study, most of the tumours were located in or near the chiasm, which is located close to the oral cavity. In addition, the pontine area is also a location where APTw values are unreliable.[44] It should be investigated if improving the acquisition parameters, such as using longer saturation pulses and thinner slices, will increase the reliability in these regions.

5 | Implementation and future perspectives

In summary, the phantom study indicates that with a simulated ratio map of the CEST effect, which represented the B_1 inhomogeneity, more homogeneous APTw maps can be created. Furthermore, APTw maps, quantified with both Lorentzian fitting as MTR asymmetry, of thirteen paediatric brain tumours did not have any relation with the clinical outcome of these patients both in the uncorrected and corrected data. However, in the APTw maps, quantified with MTR asymmetry, the average APTw value of the tumours was significantly higher than the average APTw value in normal brain tissue. Implying that tumour tissue can be investigated using APTw maps at 7T.

5.1 Clinical implementation of APTw imaging at 7T

The results of this study indicate that APTw imaging at 7T for assessing treatment outcomes in paediatric LGG does not appear to be a useful tool for radiologists when making clinical decisions. APTw imaging at 7T is not yet robust enough in children, due to movement, too little SNR and B_1 inhomogeneity. However, more research is needed to investigate the implementation of other CEST effects measured at 7T, like the NOE effect.[27] At this point APTw imaging at 7T, in addition to the conventional MRI scan, has no added value and is an additional burden for the patient. On the contrary, APTw imaging at 3T, investigated in the study of Obdeijn et al.[20], should be investigated during treatment to see if treatment effects can be evaluated in paediatric brain tumours.

5.2 Future perspectives

In future research, APTw imaging in patients with HGG gliomas should be investigated, as literature in adults has shown that LGG and HGG gliomas have different APTw values.[15, 16, 17, 18] This effect is caused by the increased cell proliferation and overexpression of proteins in HGG resulting in higher APTw values compared to LGG.[51] Furthermore, the patient cohort for the MITCH study should be expanded to provide a more thorough assessment of the applicability of APTw imaging in paediatric neuro-oncology. If these children are scanned, efforts should focus on enhancing the robustness of APTw imaging techniques. In further research, it is important to see whether findings of APTw imaging are supported by other sequences, e.g. ^{31}P MRS, in the detection of metabolic changes inside tumours.[52]

Bibliography

[1] Kim C. C. van de Ven Keupp and Jochen. Amide proton transfer weighted imaging : Advancement in molecular tumor diagnosis. 2018.

[2] SKION. Skion basisregistratie 2003-2022. 15-12-2022.

[3] D. Molanus, D. G. van Vuurden, S. E. Mir, G. J. L. Kaspers, R. J. Vermeulen, C. M. Korbijn, and W. P. Vandertop. Hersentumoren op kinderleeftijd. *Tijdschrift voor Kindergeneeskunde*, 79(5):146–155, 2012.

[4] A. Jaju, K. W. Yeom, and M. E. Ryan. Mr imaging of pediatric brain tumors. *Diagnostics (Basel)*, 12(4), 2022.

[5] A. Jaju, K. W. Yeom, and M. E. Ryan. Mr imaging of pediatric brain tumors. *Diagnostics (Basel)*, 12(4), 2022.

[6] R. H. Haslam. Clinical neurological examination of infants and children. *Handb Clin Neurol*, 111:17–25, 2013.

[7] M. A. Nuijts, I. Stegeman, T. van Seeters, M. D. Borst, C. A. M. Bennebroek, D. R. Buis, N. C. Naus, G. L. Porro, M. B. van Egmond-Ebbeling, E. S. M. Voskuil-Kerkhof, J. R. Pott, N. E. Franke, E. de Vos-Kerkhof, E. W. Hoving, A. Y. N. Schouten-van Meeteren, and S. M. Imhof. Ophthalmological findings in youths with a newly diagnosed brain tumor. *JAMA Ophthalmol*, 140(10):982–993, 2022.

[8] Y. Koenraads, K. P. Braun, D. C. van der Linden, S. M. Imhof, and G. L. Porro. Perimetry in young and neurologically impaired children: the behavioral visual field (befie) screening test revisited. *JAMA Ophthalmol*, 133(3):319–25, 2015.

[9] E. L. Greve, F. Dannheim, and D. Bakker. The peritest, a new automatic and semi-automatic perimeter. *Int Ophthalmol*, 5(3):201–14, 1982.

[10] M. A. Nuijts, S. M. Imhof, N. Veldhuis, C. C. Dekkers, A. Y. N. Schouten-van Meeteren, and I. Stegeman. The diagnostic accuracy and prognostic value of oct for the evaluation of the visual function in children with a brain tumour: A systematic review. *PLoS One*, 16(12):e0261631, 2021.

[11] J. Fangusaro, O. Witt, P. Hernaiz Driever, A. K. Bag, P. de Blank, N. Kadom, L. Kilburn, R. M. Lober, N. J. Robison, M. J. Fisher, R. J. Packer, T. Young Poussaint, L. Papusha, S. Avula, A. A. Brandes, E. Bouffet, D. Bowers, A. Artemov, M. Chintagumpala, D. Zurakowski, M. van den Bent, B. Bison, K. W. Yeom, W. Taal, and K. E. Warren. Response assessment in paediatric low-grade glioma: recommendations from the response assessment in pediatric neuro-oncology (rapno) working group. *Lancet Oncol*, 21(6):e305–e316, 2020.

[12] C. Erker, B. Tamrazi, T. Y. Poussaint, S. Mueller, D. Mata-Mbemba, E. Franceschi, A. A. Brandes, A. Rao, K. B. Haworth, P. Y. Wen, S. Goldman, G. Vezina, T. J. MacDonald, I. J. Dunkel, P. S.

Morgan, T. Jaspan, M. D. Prados, and K. E. Warren. Response assessment in paediatric high-grade glioma: recommendations from the response assessment in pediatric neuro-oncology (rapno) working group. *Lancet Oncol*, 21(6):e317–e329, 2020.

[13] S. C. Thust, M. J. van den Bent, and M. Smits. Pseudoprogression of brain tumors. *J Magn Reson Imaging*, 48(3):571–89, 2018.

[14] B. Wu, G. Warnock, M. Zaiss, C. Lin, M. Chen, Z. Zhou, L. Mu, D. Nanz, R. Tuura, and G. Delso. An overview of cest mri for non-mr physicists. *EJNMMI Phys*, 3(1):19, 2016.

[15] C. Su, C. Liu, L. Zhao, J. Jiang, J. Zhang, S. Li, W. Zhu, and J. Wang. Amide proton transfer imaging allows detection of glioma grades and tumor proliferation: Comparison with ki-67 expression and proton mr spectroscopy imaging. *AJNR Am J Neuroradiol*, 38(9):1702–1709, 2017.

[16] O. Togao, T. Yoshiura, J. Keupp, A. Hiwatashi, K. Yamashita, K. Kikuchi, Y. Suzuki, S. O. Suzuki, T. Iwaki, N. Hata, M. Mizoguchi, K. Yoshimoto, K. Sagiyama, M. Takahashi, and H. Honda. Amide proton transfer imaging of adult diffuse gliomas: correlation with histopathological grades. *Neuro Oncol*, 16(3):441–8, 2014.

[17] J. Zhou, H. Zhu, M. Lim, L. Blair, A. Quinones-Hinojosa, S. A. Messina, C. G. Eberhart, M. G. Pomper, J. Laterra, P. B. Barker, P. C. van Zijl, and J. O. Blakeley. Three-dimensional amide proton transfer mr imaging of gliomas: Initial experience and comparison with gadolinium enhancement. *J Magn Reson Imaging*, 38(5):1119–28, 2013.

[18] J. Zhang, W. Zhu, R. Tain, X. J. Zhou, and K. Cai. Improved differentiation of low-grade and high-grade gliomas and detection of tumor proliferation using apt contrast fitted from z-spectrum. *Mol Imaging Biol*, 20(4):623–631, 2018.

[19] D. Cheng, Z. Zhuo, P. Zhang, L. Qu, Y. Duan, X. Xu, C. Xie, X. Liu, S. Haller, F. Barkhof, L. Zhang, and Y. Liu. Amide proton transfer-weighted imaging of pediatric brainstem glioma and its predicted value for h3 k27 alteration. *Acta Radiol*, 64(11):2922–2930, 2023.

[20] I. V. Obdeijn, E. C. Wiegers, L. Alic, S. L. A. Plasschaert, M. E. G. Kranendonk, H. M. Hoogduin, D. W. J. Klomp, J. P. Wijnen, and M. H. Lequin. Amide proton transfer weighted imaging in pediatric neuro-oncology: initial experience. *NMR Biomed*, 2024.

[21] P. C. van Zijl and N. N. Yadav. Chemical exchange saturation transfer (cest): what is in a name and what isn't? *Magn Reson Med*, 65(4):927–48, 2011.

[22] F. Kogan, H. Hariharan, and R. Reddy. Chemical exchange saturation transfer (cest) imaging: Description of technique and potential clinical applications. *Curr Radiol Rep*, 1(2):102–114, 2013.

[23] Harvey PR Brink J van den Keupp J, Baltes C. Parallel rf transmission based mri technique for highly sensitive detection of amide proton transfer in the human brain at 3 t. *Proc Intl Soc Mag Reson Med*, 19, 2011.

[24] Keupp J et al Hoogduin H, Khlebnikov V. Semi continuous wave cest with alternating sets of 4 transmit channels at 7t. *MAGMA*, 30:S1 – S152, 2017.

[25] L. Zhang, C. Xu, Z. Li, J. Sun, X. Wang, B. Hou, and Y. Zhao. Chemical exchange saturation transfer (cest) magnetic resonance imaging (mri) quantification of transient ischemia using a combination method of 5-pool lorentzian fitting and inverse z-spectrum analysis. *Quant Imaging Med Surg*, 13(3):1860–1873, 2023.

[26] J. Windschuh, M. Zaiss, J. E. Meissner, D. Paech, A. Radbruch, M. E. Ladd, and P. Bachert. Correction of b1-inhomogeneities for relaxation-compensated cest imaging at 7 t. *NMR Biomed*, 28(5):529–37, 2015.

[27] H. Y. Heo, C. K. Jones, J. Hua, N. Yadav, S. Agarwal, J. Zhou, P. C. van Zijl, and J. J. Pillai. Whole-brain amide proton transfer (apt) and nuclear overhauser enhancement (noe) imaging in glioma patients using low-power steady-state pulsed chemical exchange saturation transfer (cest) imaging at 7t. *J Magn Reson Imaging*, 44(1):41–50, 2016.

[28] E. Krikken, V. Khlebnikov, M. Zaiss, R. A. Jibodh, P. J. van Diest, P. R. Luijten, D. W. J. Klomp, H. W. M. van Laarhoven, and J. P. Wijnen. Amide chemical exchange saturation transfer at 7 t: a possible biomarker for detecting early response to neoadjuvant chemotherapy in breast cancer patients. *Breast Cancer Res*, 20(1):51, 2018.

[29] M. Zaiss, J. Windschuh, D. Paech, J. E. Meissner, S. Burth, B. Schmitt, P. Kickingereder, B. Wiestler, W. Wick, M. Bendszus, H. P. Schlemmer, M. E. Ladd, P. Bachert, and A. Radbruch. Relaxation-compensated cest-mri of the human brain at 7t: Unbiased insight into noe and amide signal changes in human glioblastoma. *Neuroimage*, 112:180–188, 2015.

[30] J. P. Stockmann and L. L. Wald. In vivo b(0) field shimming methods for mri at 7t. *Neuroimage*, 168:71–87, 2018.

[31] M. Park, H. Noh, and N. Park. Mitigation of b(1)(+) inhomogeneity for ultra-high-field magnetic resonance imaging: hybrid mode shaping with auxiliary em potential. *Sci Rep*, 10(1):11752, 2020.

[32] Z. Zhang, C. Y. Yip, W. Grissom, D. C. Noll, F. E. Boada, and V. A. Stenger. Reduction of transmitter b1 inhomogeneity with transmit sense slice-select pulses. *Magn Reson Med*, 57(5):842–7, 2007.

[33] Q. X. Yang, J. Wang, X. Zhang, C. M. Collins, M. B. Smith, H. Liu, X. H. Zhu, J. T. Vaughan, K. Ugurbil, and W. Chen. Analysis of wave behavior in lossy dielectric samples at high field. *Magn Reson Med*, 47(5):982–9, 2002.

[34] C. M. Collins, W. Liu, W. Schreiber, Q. X. Yang, and M. B. Smith. Central brightening due to constructive interference with, without, and despite dielectric resonance. *J Magn Reson Imaging*, 21(2):192–6, 2005.

[35] P. Schuenke, J. Windschuh, V. Roeloffs, M. E. Ladd, P. Bachert, and M. Zaiss. Simultaneous mapping of water shift and b(1) (wasabi)-application to field-inhomogeneity correction of cest mri data. *Magn Reson Med*, 77(2):571–580, 2017.

[36] K. Nehrke and P. Bornert. Dream–a novel approach for robust, ultrafast, multislice b(1) mapping. *Magn Reson Med*, 68(5):1517–26, 2012.

[37] P. Orlowski, M. Chappell, C. S. Park, V. Grau, and S. Payne. Modelling of ph dynamics in brain cells after stroke. *Interface Focus*, 1(3):408–16, 2011.

[38] JM. Hoogduin. Internal report safety documentation. Report, 2021.

[39] Michael R. Thompson Ramesh Venkatesan E. Mark Haacke, Robert W. Brown. *Magnetization, Relaxation, and the Bloch Equation*, book section 4. Wiley, 1999.

[40] D. E. Woessner, S. Zhang, M. E. Merritt, and A. D. Sherry. Numerical solution of the bloch equations provides insights into the optimum design of paracest agents for mri. *Magn Reson Med*, 53(4):790–9, 2005.

[41] V. Khlebnikov, W. J. M. van der Kemp, H. Hoogduin, D. W. J. Klomp, and J. J. Prompers. Analysis of chemical exchange saturation transfer contributions from brain metabolites to the z-spectra at various field strengths and ph. *Sci Rep*, 9(1):1089, 2019.

[42] R. Simpson, G. A. Devenyi, P. Jezzard, T. J. Hennessy, and J. Near. Advanced processing and simulation of mrs data using the fid appliance (fid-a)-an open source, matlab-based toolkit. *Magn Reson Med*, 77(1):23–33, 2017.

[43] Y. Msayib, G. W. J. Harston, Y. K. Tee, F. Sheerin, N. P. Blockley, T. W. Okell, P. Jezzard, J. Kennedy, and M. A. Chappell. Quantitative cest imaging of amide proton transfer in acute ischaemic stroke. *Neuroimage Clin*, 23:101833, 2019.

[44] I.V. Obdeijn. *APTw imaging in paediatric brain tumours: no waste of time and energy.* Thesis, 2021.

[45] N. Zhukova, R. Rajagopal, A. Lam, L. Coleman, P. Shipman, T. Walwyn, M. Williams, M. Sullivan, M. Campbell, K. Bhatia, N. G. Gottardo, and J. R. Hansford. Use of bevacizumab as a single agent or in adjunct with traditional chemotherapy regimens in children with unresectable or progressive low-grade glioma. *Cancer Med*, 8(1):40–50, 2019.

[46] K. Kamimura, M. Nakajo, M. Gohara, K. Kawaji, M. Bohara, Y. Fukukura, H. Uchida, K. Tabata, T. Iwanaga, Y. Akamine, J. Keupp, T. Fukami, and T. Yoshiura. Differentiation of hemangioblastoma from brain metastasis using mr amide proton transfer imaging. *J Neuroimaging*, 32(5):920–929, 2022.

[47] M. A. Nuijts, S. M. Imhof, N. Veldhuis, C. C. Dekkers, A. Y. N. Schouten-van Meeteren, and I. Stegeman. The diagnostic accuracy and prognostic value of oct for the evaluation of the visual function in children with a brain tumour: A systematic review. *PLoS One*, 16(12):e0261631, 2021.

[48] V. Khlebnikov, D. Polders, J. Hendrikse, P. A. Robe, E. H. Voormolen, P. R. Luijten, D. W. Klomp, and H. Hoogduin. Amide proton transfer (apt) imaging of brain tumors at 7 t: The role of tissue water t(1) -relaxation properties. *Magn Reson Med*, 77(4):1525–1532, 2017.

[49] H. Y. Heo, C. K. Jones, J. Hua, N. Yadav, S. Agarwal, J. Zhou, P. C. van Zijl, and J. J. Pillai. Whole-brain amide proton transfer (apt) and nuclear overhauser enhancement (noe) imaging in glioma patients using low-power steady-state pulsed chemical exchange saturation transfer (cest) imaging at 7t. *J Magn Reson Imaging*, 44(1):41–50, 2016.

[50] O. Afacan, B. Erem, D. P. Roby, N. Roth, A. Roth, S. P. Prabhu, and S. K. Warfield. Evaluation of motion and its effect on brain magnetic resonance image quality in children. *Pediatr Radiol*, 46(12):1728–1735, 2016.

[51] J. Zhou, H. Y. Heo, L. Knutsson, P. C. M. van Zijl, and S. Jiang. Apt-weighted mri: Techniques, current neuro applications, and challenging issues. *J Magn Reson Imaging*, 50(2):347–364, 2019.

[52] A. Korzowski, N. Weckesser, V. L. Franke, J. Breitling, S. Goerke, H. P. Schlemmer, M. E. Ladd, P. Bachert, and D. Paech. Mapping an extended metabolic profile of gliomas using high-resolution (31)p mrsi at 7t. *Front Neurol*, 12:735071, 2021.

A | Lorentzian fitting parameters

The APTw maps can be subtracted from the z-spectrum by using Lorentzian fitting metrics. To apply this metric, Parameters need to be predefined. The parameters are defined in an earlier graduation project.[44]

Table A.1: Fitting parameters for 6-pool Lorentzian fitting. A is the amplitude, δ is the chemical shift in ppm and Γ is the FWHM in ppm.

	Start	Lower	Upper
A_{water}	0.9	0.02	1.0
Γ_{water}	1.4	0.3	10.0
δ_{water}	0.0	-1.0	1.0
A_{MT}	0.1	0.0	1.0
Γ_{MT}	25	10	100
δ_{MT}	-2.0	-4.0	-2.0
A_{amide}	0.025	0.0	0.2
Γ_{amide}	0.5	0.4	3.0
δ_{amide}	3.5	3.0	4.0
A_{NOE}	0.02	0.0	0.4
Γ_{NOE}	3.0	1.0	5.0
δ_{NOE}	-3.5	-4.5	-2.0
A_{amine}	0.01	0.0	0.2
Γ_{amine}	0.5	0.4	3.0
δ_{amine}	2.2	1.0	2.5
$A_{hydroxyl}$	0.01	0.0001	0.1
$\Gamma_{hydroxyl}$	0.2	0.0	0.9
$\delta_{hydroxyl}$	0.9	0.8	1.0

B | Bloch equations

The Bloch equations for a two-pool model, where pool A is the bulk water and pool B the amides.

$$\frac{dM_x^a}{dt} = -(\omega_a - \omega)M_y^a - k_{2a}M_x^a + C_bM_x^b \tag{B.1}$$

$$\frac{dM_x^b}{dt} = -(\omega_b - \omega)M_y^b - k_{2b}M_x^b + C_aM_x^a \tag{B.2}$$

$$\frac{dM_y^a}{dt} = -(\omega_a - \omega)M_x^a - k_{2a}M_y^a + C_bM_y^b - \omega_1M_z^a \tag{B.3}$$

$$\frac{dM_y^b}{dt} = -(\omega_b - \omega)M_x^b - k_{2b}M_y^b + C_aM_y^a - \omega_1M_z^b \tag{B.4}$$

$$\frac{dM_z^a}{dt} = \frac{M_0^a}{T_{1a}} - k_{1a}M_z^a + C_bM_z^b + \omega_1M_y^a \tag{B.5}$$

$$\frac{dM_z^b}{dt} = \frac{M_0^b}{T_{1b}} - k_{1b}M_z^b + C_aM_z^a + \omega_1M_y^b \tag{B.6}$$

where

$$k_{1a} = \frac{1}{T_{1a}} + C_a \tag{B.7}$$

$$k_{2a} = \frac{1}{T_{2a}} + C_a \tag{B.8}$$

and T_{1a} and T_{2a} are the relaxation times of pool A in the absence of exchange, ω is the frequency of the RF irradiation, ω_a is the Larmor frequency of pool A, ω_1 is the nutation rate of the RF irradiation, C_a is the transition rate of A spins leaving pool A, and k_a is the exchange rate of pool A. These definitions are similar for pool B.[40]

C | Mean and standard deviation tubes in the phantom

Table C.1: The mean APTw value and standard deviation for (a) all the tubes and (b)(c)(d)(e) each tube individually.

All tubes	Mean	Standard deviation
Before correction	0.1032	0.0248
After correction	0.0703	0.0203

(a)

Tube 1	Mean	Standard deviation
Before correction	0.1003	0.0232
After correction	0.0652	0.0147

(b)

Tube 2	Mean	Standard deviation
Before correction	0.0958	0.0201
After correction	0.0628	0.0134

(c)

Tube 3	Mean	Standard deviation
Before correction	0.1022	0.0235
After correction	0.0696	0.0200

(d)

Tube 4	Mean	Standard deviation
Before correction	0.1009	0.0206
After correction	0.0678	0.0142

(e)

Tube 5	Mean	Standard deviation
Before correction	0.1013	0.0232
After correction	0.0665	0.0148

D | Registration parameters FLAIR image to CEST coordinate system

```
//ImageTypes
(FixedInternalImagePixelType "float")
(FixedImageDimension 3)
(MovingInternalImagePixelType "float")
(MovingImageDimension 3)

    (UseDirectionCosines "true")

    //Components
(Registration "MultiResolutionRegistration")
(FixedImagePyramid "FixedRecursiveImagePyramid")
(MovingImagePyramid "MovingRecursiveImagePyramid")

    (Interpolator "BSplineInterpolator")
(Metric "AdvancedMattesMutualInformation")
(Optimizer "AdaptiveStochasticGradientDescent")
(ResampleInterpolator "FinalBSplineInterpolator")
(Resampler "DefaultResampler")
(Transform "EulerTransform")

    (ErodeMask "false")
(NumberOfResolutions 6)

    (FixedImagePyramidSchedule 16 16 2 8 8 1 4 4 1 2 2 1 1 1 1 1 1 1)
//(MovingImagePyramidSchedule 32 32 24 16 16 12 8 8 12 4 4 6 2 2 2 1 1 1)
//(MovingImagePyramidSchedule 32 16 24 16 8 12 8 4 12 4 2 6 2 1 2 1 1 1)
(MovingImagePyramidSchedule 32 16 8 16 8 4 8 4 4 4 2 2 2 1 1 1 1 1)

    (HowToCombineTransforms "Compose")
(AutomaticParameterEstimation "true")
(AutomaticTransformInitialization "true")
(AutomaticScalesEstimation "true")
(AutomaticTransformInitializationMethod "CenterOfGravity" )

    (WriteTransformParametersEachIteration "false")
(WriteResultImage "true")
(CompressResultImage "false")
(WriteTransformParametersEachResolution "false")
```

```
(ShowExactMetricValue "false")
(ResultImagePixelType "short")
(ResultImageFormat "mhd")

    //Maximum number of iterations in each resolution level:
(MaximumNumberOfIterations 2000)

    //Number of grey level bins in each resolution level:
(NumberOfHistogramBins 32)
(NumberOfMovingHistogramBins 32)
(NumberOfFixedHistogramBins 32)

    //Number of spatial samples used to compute the mutual information in each resolution level:
(ImageSampler "RandomCoordinate")
(NumberOfSpatialSamples 5000)
(MaximumNumberOfSamplingAttempts 15)
(NewSamplesEveryIteration "true")
(CheckNumberOfSamples "true")

    //Order of B-Spline interpolation used in each resolution level:
(BSplineInterpolationOrder 3)

    //Order of B-Spline interpolation used for applying the final deformation:
(FinalBSplineInterpolationOrder 3)

    //Default pixel value for pixels that come from outside the picture:
(DefaultPixelValue 0)
```

E | Clinical outcome

E.1 OCT

The OCT data of patient 1, 2, 3, 4, 7, 8, 10, and 13. In patient 8 and 13 only two exams were performed.

Table E.1: OCT data of patient 1

OCT RNFL				
	Baseline exam	follow-up exam 1	follow-up exam 2	follow-up exam 3
OD	70	67	73	74
OS	61	63	62	63

OCT GCL				
	Baseline exam	follow-up exam 1	follow-up exam 2	follow-up exam 3
OD average	61	63	64	60
OD minimum	52	54	54	53
OS average	61	62	63	61
OS minimum	53	50	53	49

Table E.2: OCT data of patient 2

OCT RNFL			
	Baseline exam	follow-up exam 1	follow-up exam 2
OD	72	70	68
OS	71	69	70

OCT GCL			
	Baseline exam	follow-up exam 1	follow-up exam 2
OD average	74	73	74
OD minimum	47	45	45
OS average	67	64	67
OS minimum	46	43	47

Table E.3: OCT data of patient 3

OCT RNFL			
	Baseline exam	follow-up exam 1	follow-up exam 2
OD	55	56	52
OS	53	52	52

OCT GCL			
	Baseline exam	follow-up exam 1	follow-up exam 2
OD average	49	48	48
OD minimum	41	40	39
OS average	52	52	52
OS minimum	48	48	47

Table E.4: OCT data of patient4

OCT RNFL				
	Baseline exam	follow-up exam 1	follow-up exam 2	follow-up exam 3
OD	78	76	78	77
OS	53	66	62	68

OCT GCL				
	Baseline exam	follow-up exam 1	follow-up exam 2	follow-up exam 3
OD average	72	73	73	73
OD minimum	56	54	55	55
OS average	52	52	53	54
OS minimum	47	46	47	49

Table E.5: OCT data of patient 7

OCT RNFL				
	Baseline exam	follow-up exam 1	follow-up exam 2	follow-up exam 3
OD	82	90	81	79
OS	74	77	74	67

OCT GCL				
	Baseline exam	follow-up exam 1	follow-up exam 2	follow-up exam 3
OD average	70	72	68	68
OD minimum	57	59	57	56
OS average	67	66	65	65
OS minimum	62	60	59	60

Table E.6: OCT data of patient 8

OCT RNFL		
	follow-up exam 1	follow-up exam 2
OD	x	x
OS	x	56

OCT GCL		
	follow-up exam 1	follow-up exam 2
OD average	x	40
OD minimum	x	32
OS average	50	x
OS minimum	44	x

Table E.7: OCT data of patient 10

OCT RNFL			
	Baseline exam	follow-up exam 1	follow-up exam 2
OD	51	56	55
OS	57	51	53

OCT GCL			
	Baseline exam	follow-up exam 1	follow-up exam 2
OD average	56	54	56
OD minimum	50	50	50
OS average	55	56	54
OS minimum	50	50	49

Table E.8: OCT data of patient 13

OCT RNFL		
	Baseline	follow-up exam 1
OD	76	77
OS	92	89

OCT GCL		
	Baseline	follow-up exam 1
OD average	59	59
OD minimum	53	52
OS average	66	66
OS minimum	51	51

E.2 Radiology

Table E.9: Dimensions (LR x AP x FH; in mm) of the tumor in each patient over time

	Baseline	Follow-up1	Follow-up 2
Patient 1	38.1 x 21.1 x 23.3	38.4 x 21.7 x 24.5	36.9 x 24.9 x 26.4
Patient 2	23.1 x 25.7 x 19.1	27.7 x 26.7 x 19.3	27.8 x 29.5 x 22.0
Patient 3	17.1 x 19.8 x 16.1	16.1 x 19.6 x 14.7	16.6 x 18.6 x 16.1
Patient 4	22.1 x 34.0 x 18.8	21.6 x 33.2 x 19.4	23.2 x 33.3 x 20.9
Patient 5	34.4 x 53.7 x 66.1	32.8 x 52.0 x 66.5	32.8 x 49.6 x 58.5
Patient 6	26.3 x 13.6 x 8.0	22.2 x 13.2 x 7.9	22.6 x 13.2 x 7.8
Patient 7	20.9 x 9.9 x 8.7	20.0 x 8.5 x 8.0	20.9 x 10.3 x 8.1
Patient 8	11.4 x 13.7 x 9.5	11.7 x 9.5 x 9.0	13.4 x 11.8 x 10.0
Patient 9	7.6 x 10.0 x 10.3	3.0 x 4.9 x 5.8	2.9 x 4.8 x 5.5
Patient 10	71.5 x 28.0 x 44.2	72.9 x 27.5 x 46.3	71.3 x 26.9 x 46.2
Patient 11	56.2 x 49.6 x 36.4	21.3 x 29.2 x 24.8	26.5 x 31.3 x 28.7
Patient 12	19.2 x 26.0 x 22.1	21.3 x 29.2 x 24.8	26.5 x 31.3 x 28.7
Patient 13	22.6 x 16.6 x 22.1	23.3 x 20.3 x 21.0	23.2 x 17.5 x 21.4

Table E.10: Volumes (in cm^3) of the tumor masks made for the APTw analysis.

	Baseline	Follow-up1	Follow-up 2
Patient 1	18.33	18.88	16.65
Patient 2	7.02	5.41	8.27
Patient 3	5.41	6.85	6.10
Patient 4	13.23	12.87	11.84
Patient 5	26.77	25.15	28.21
Patient 6	2.34	2.49	1.36
Patient 7	0.97	1.64	1.08
Patient 8	0.53	0.65	1.03
Patient 9	9.48	5.78	5.98
Patient 10	73.65	85.79	73.04
Patient 11	49.31	41.41	45.31
Patient 12	11.31	6.85	12.06
Patient 13	2.76	4.87	4.32

F | Lorentzian fit figures of all patients

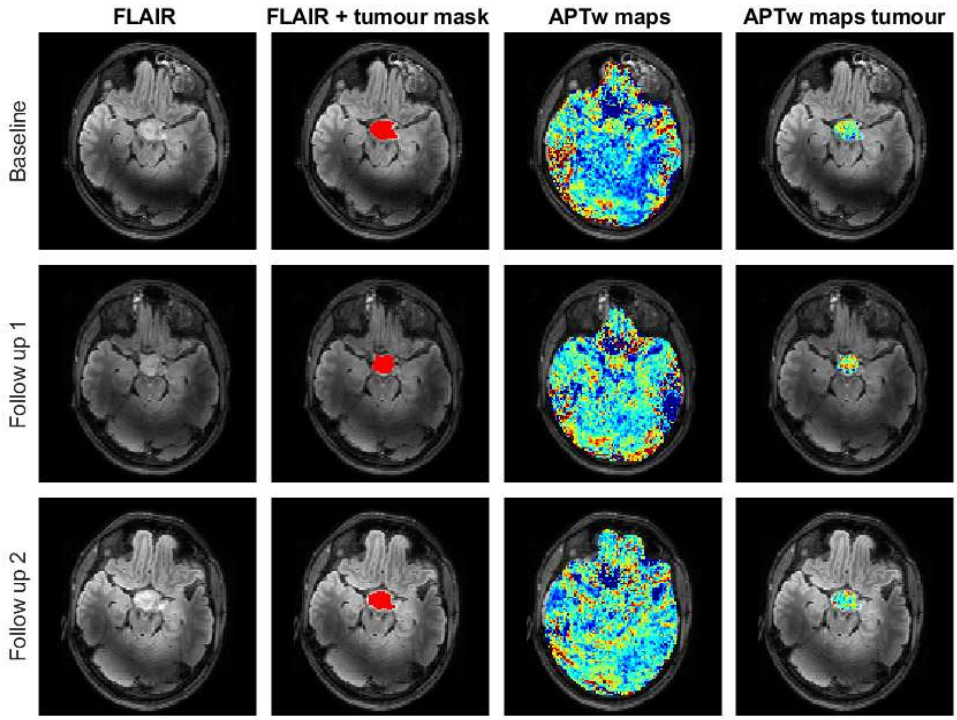

Figure F.1: Example of APTw maps quantified with Lorentzian fitting of patient 1.

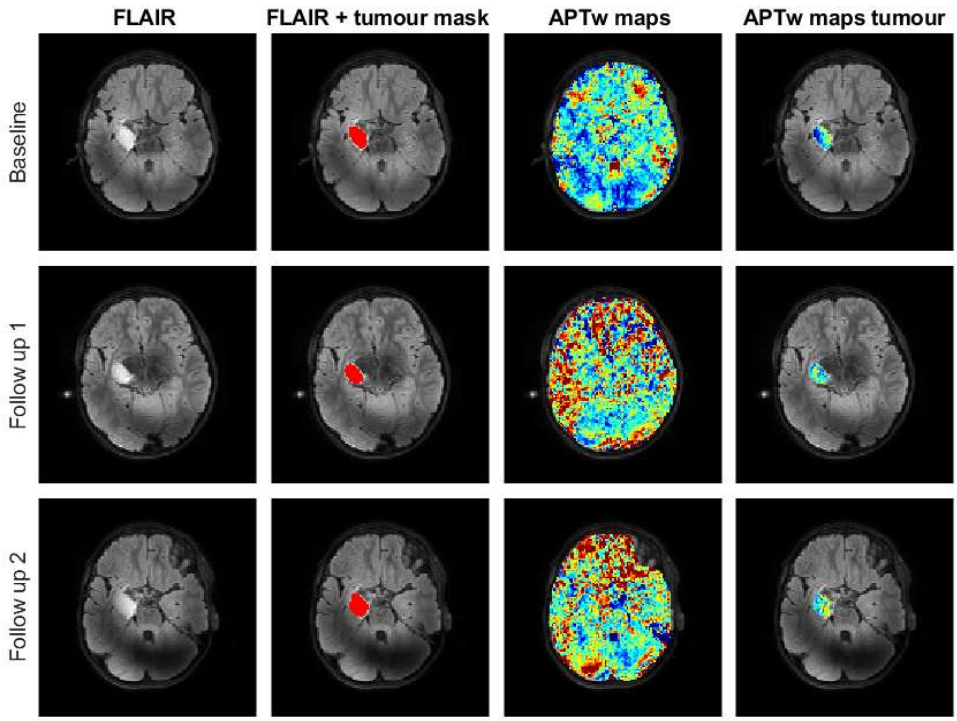

Figure F.2: Example of APTw maps quantified with Lorentzian fitting of patient 2.

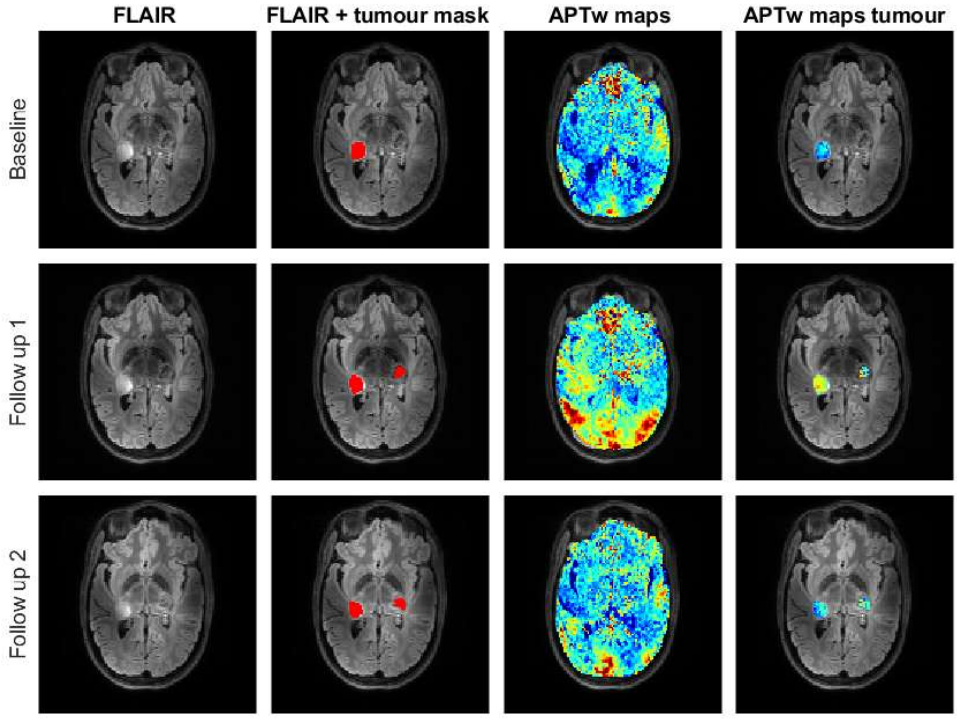

Figure F.3: Example of APTw maps quantified with Lorentzian fitting of patient 3.

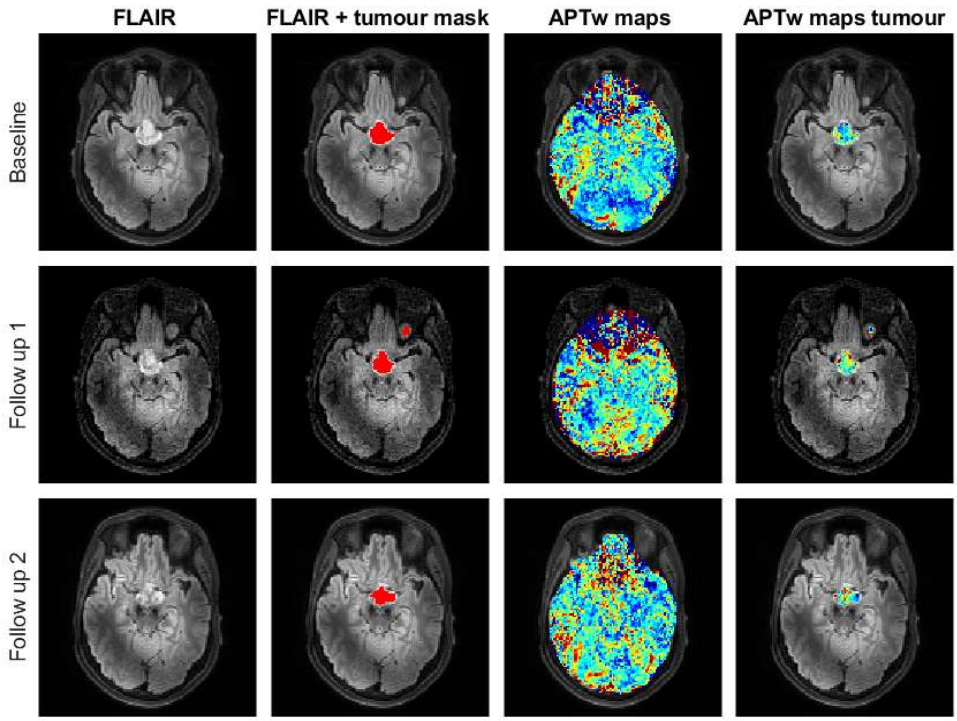

Figure F.4: Example of APTw maps quantified with Lorentzian fitting of patient 4.

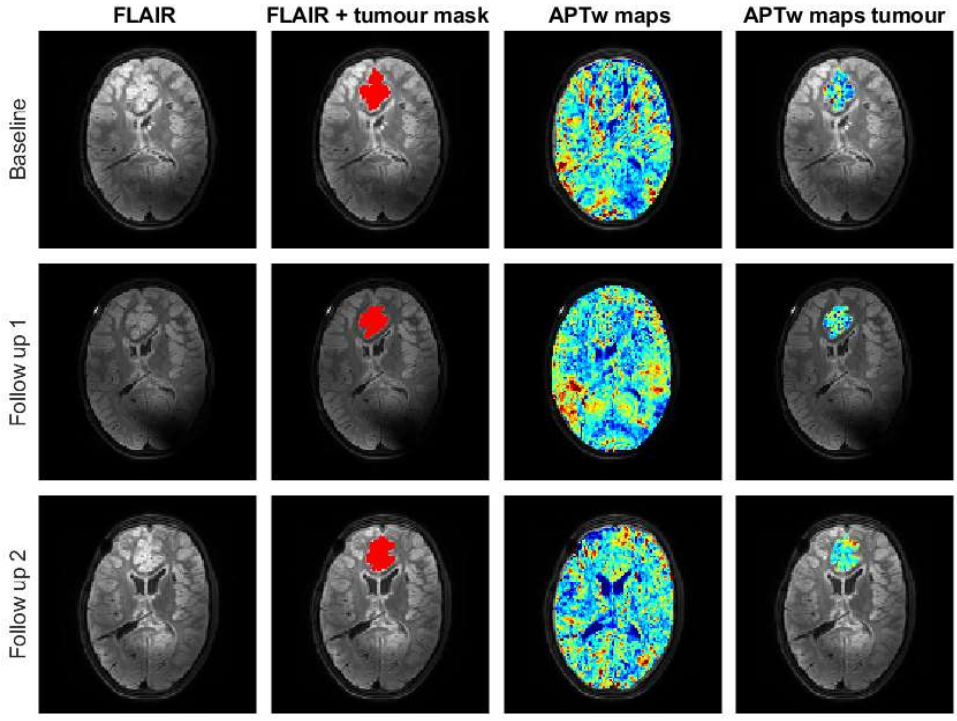

Figure F.5: Example of APTw maps quantified with Lorentzian fitting of patient 5.

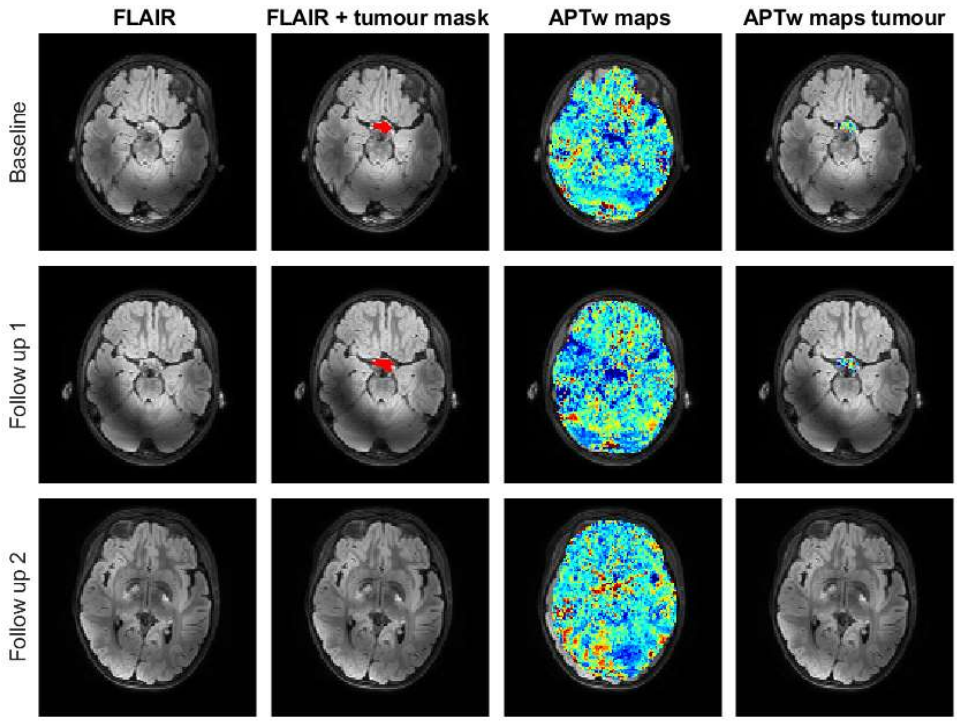

Figure F.6: Example of APTw maps quantified with Lorentzian fitting of patient 6.

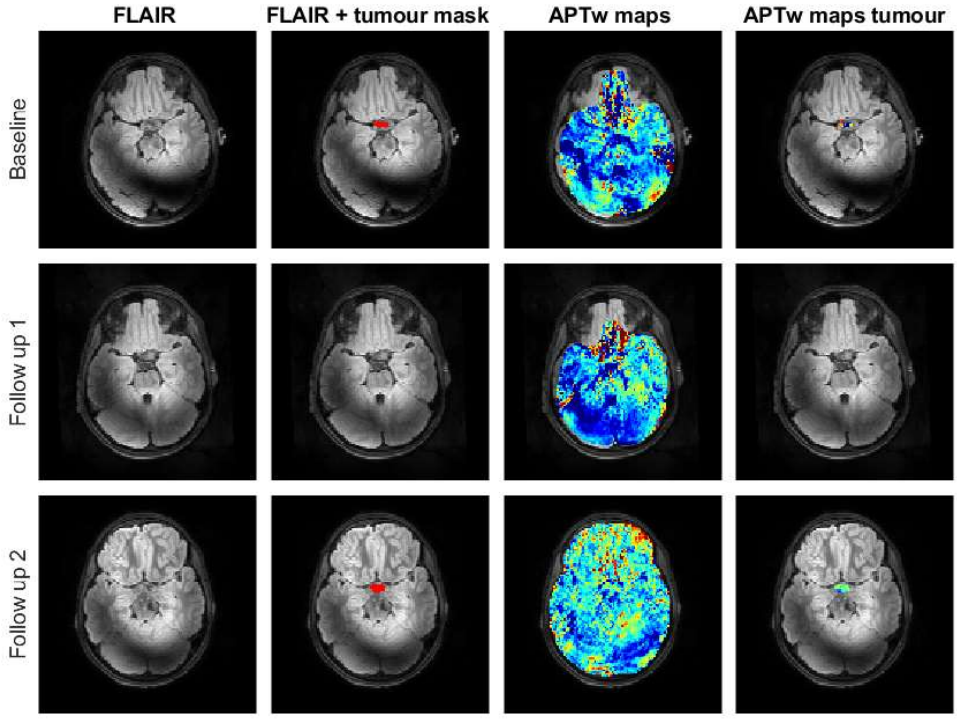

Figure F.7: Example of APTw maps quantified with Lorentzian fitting of patient 7.

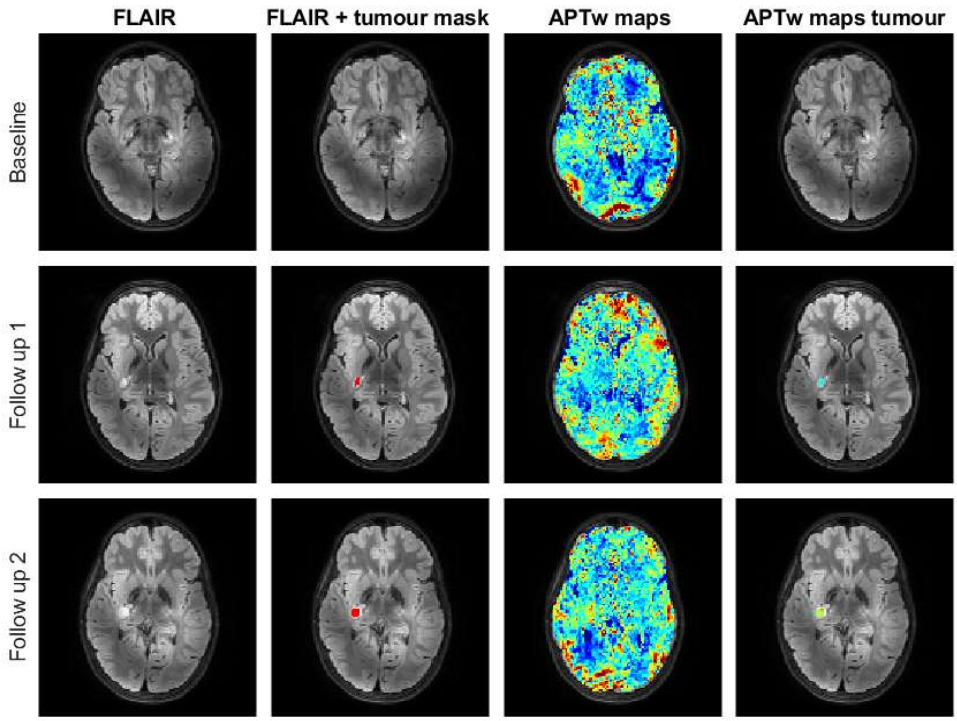

Figure F.8: Example of APTw maps quantified with Lorentzian fitting of patient 8.

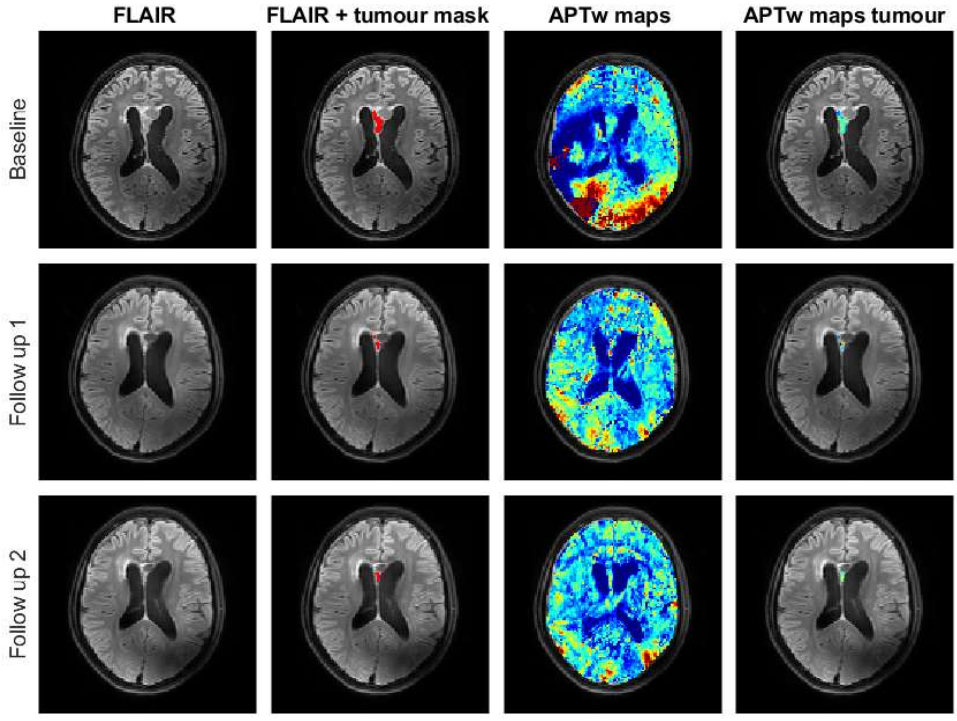

Figure F.9: Example of APTw maps quantified with Lorentzian fitting of patient 9.

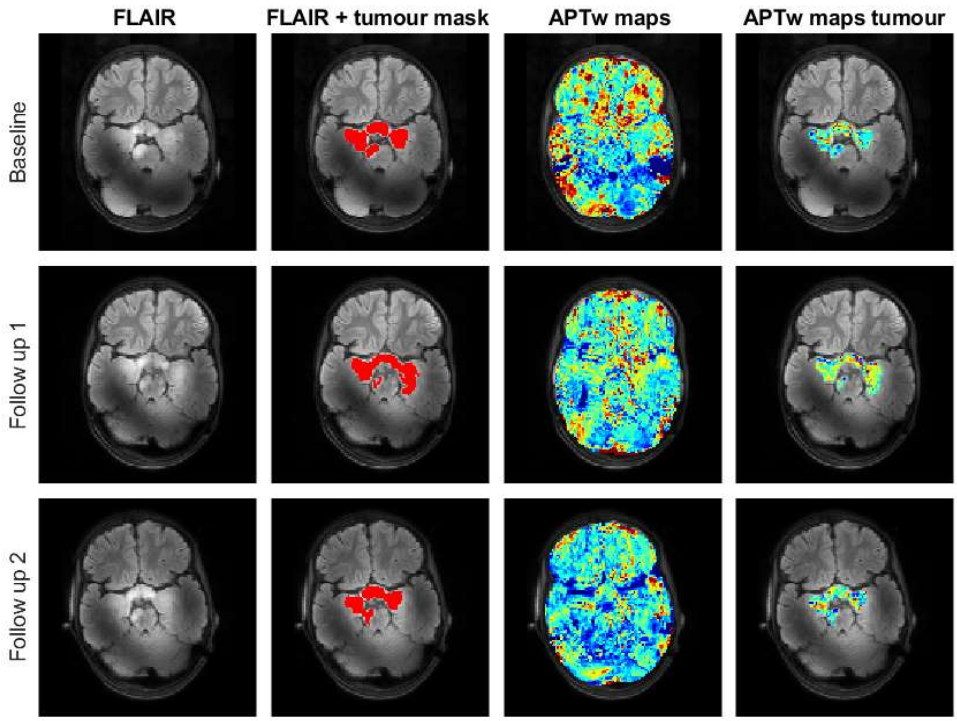

Figure F.10: Example of APTw maps quantified with Lorentzian fitting of patient 10.

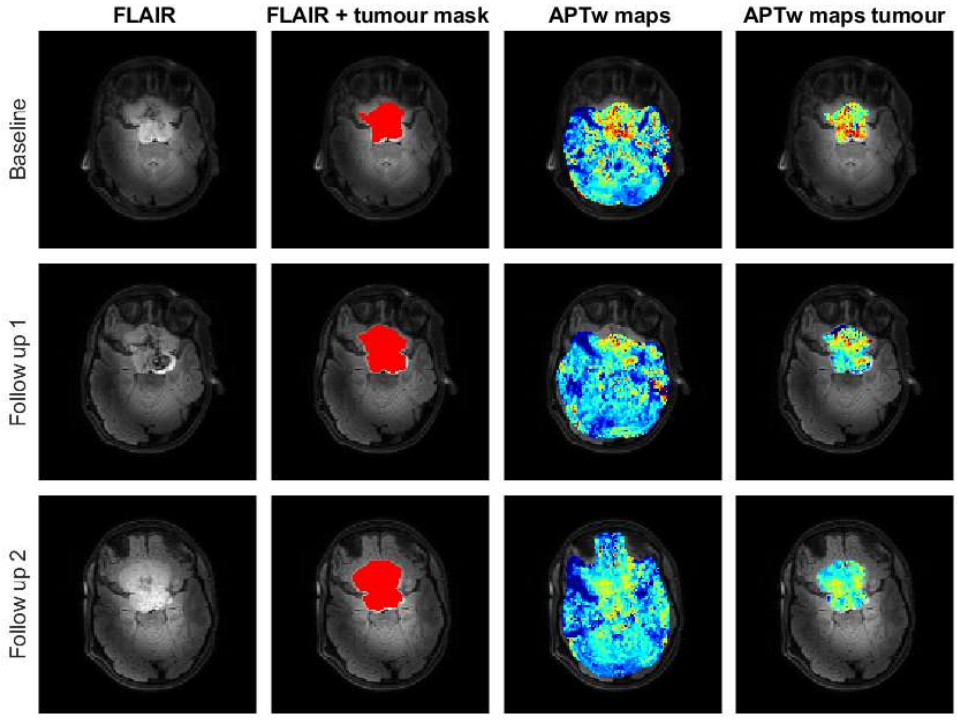

Figure F.11: Example of APTw maps quantified with Lorentzian fitting of patient 11.

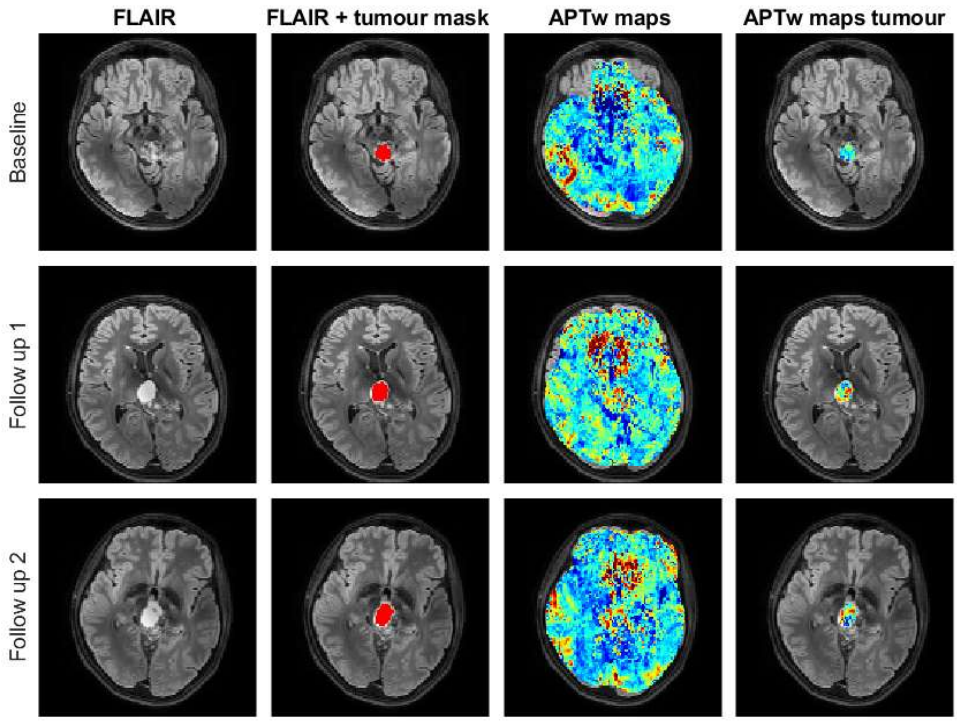

Figure F.12: Example of APTw maps quantified with Lorentzian fitting of patient 12.

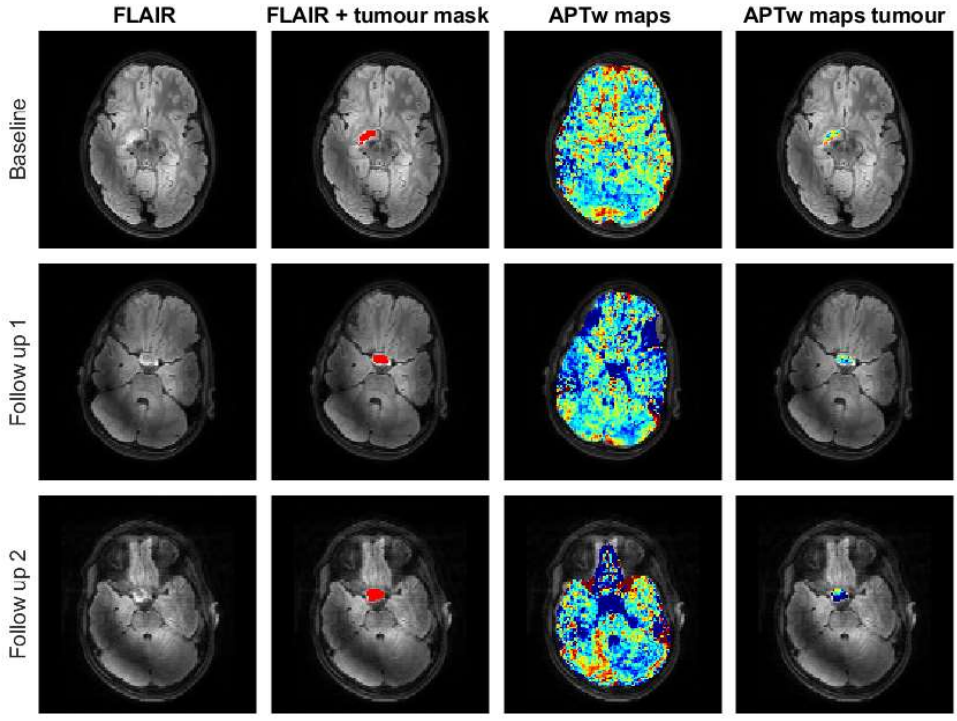

Figure F.13: Example of APTw maps quantified with Lorentzian fitting of patient 13.

G | MTRasym figures of all patients

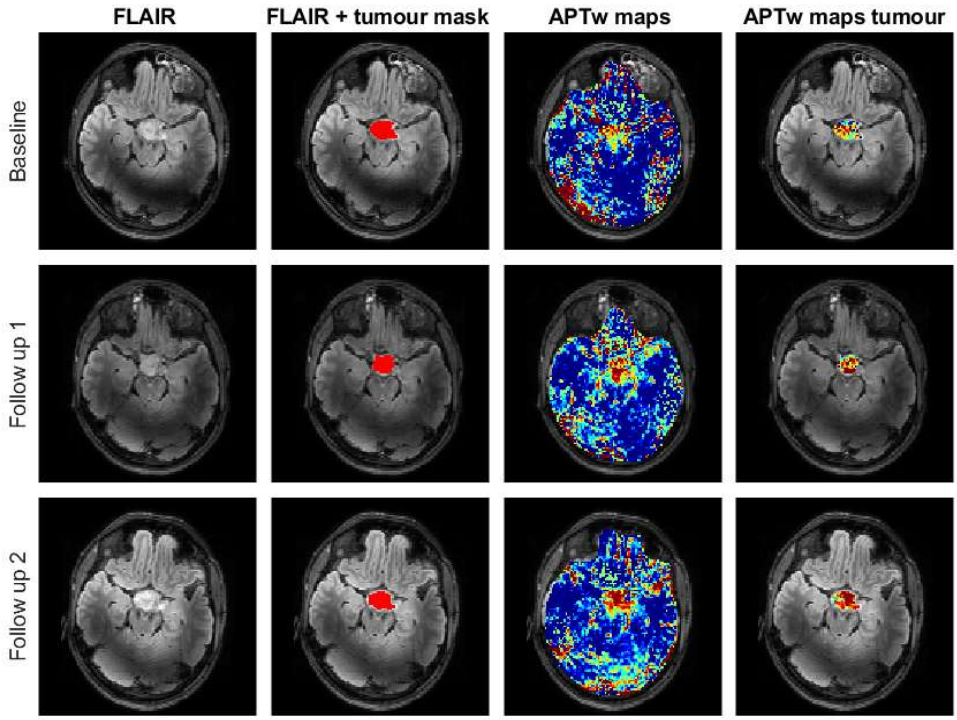

Figure G.1: Example of APTw maps quantified with MTRasym of patient 1.

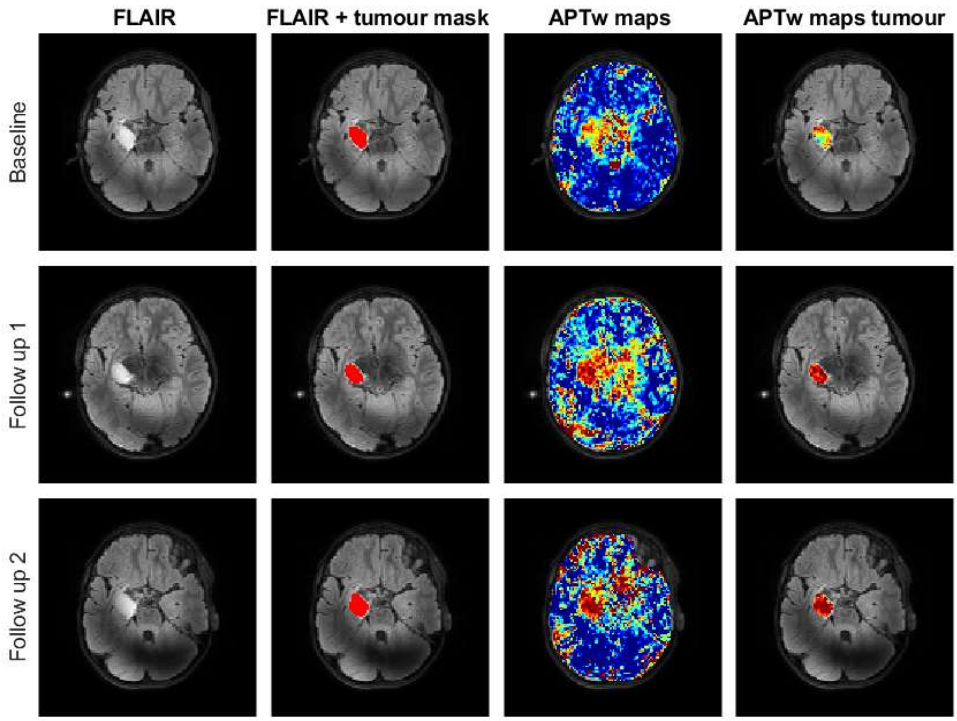

Figure G.2: Example of APTw maps quantified with MTRasym of patient 2.

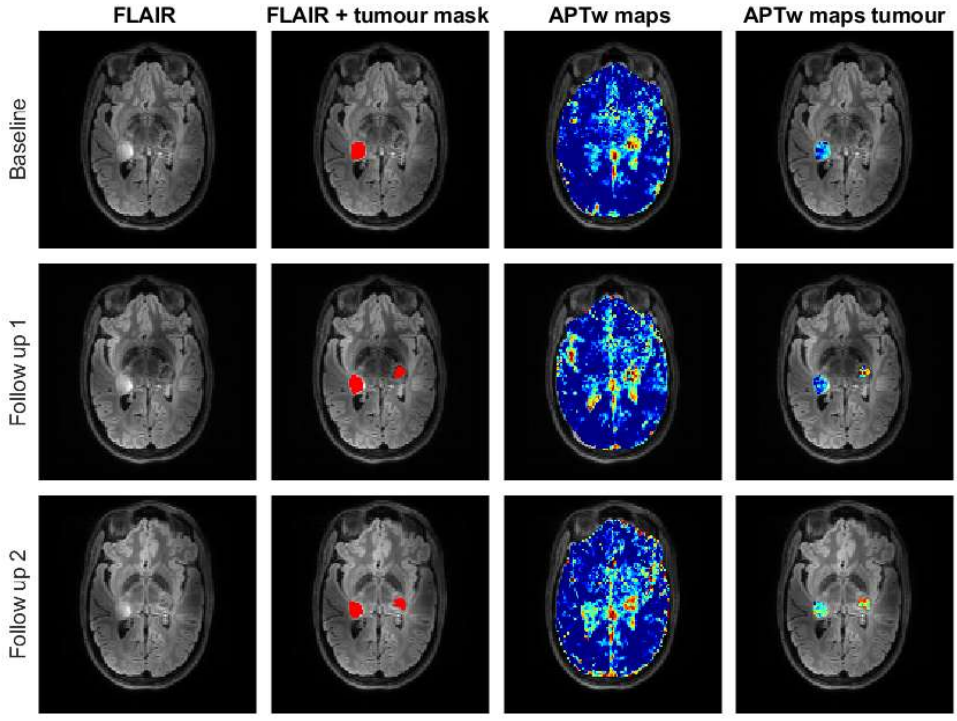

Figure G.3: Example of APTw maps quantified with MTRasym of patient 3.

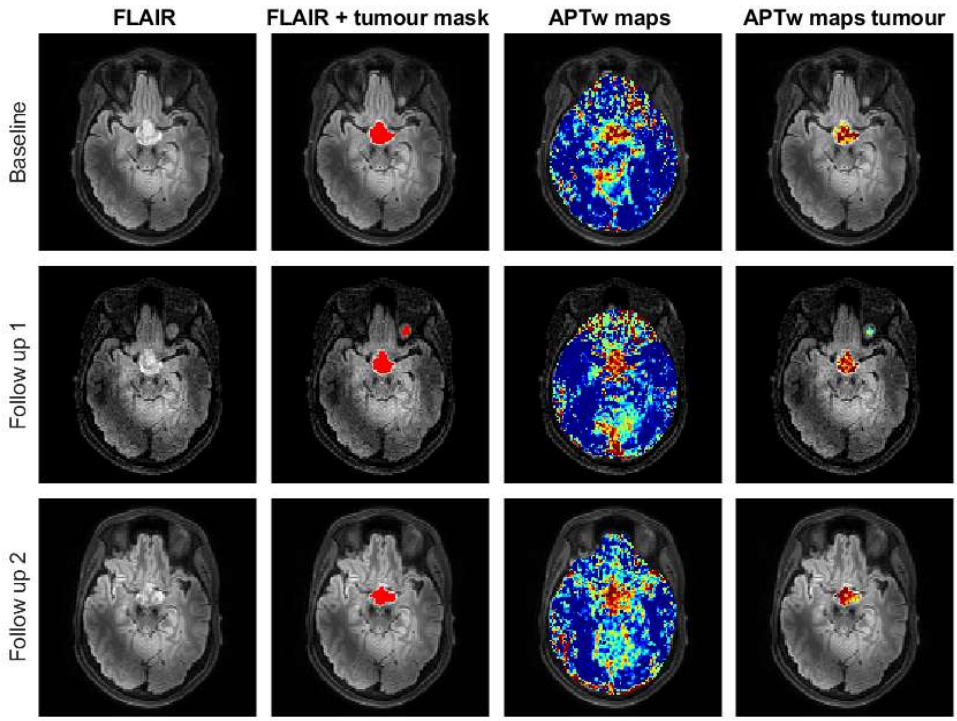

Figure G.4: Example of APTw maps quantified with MTRasym of patient 4.

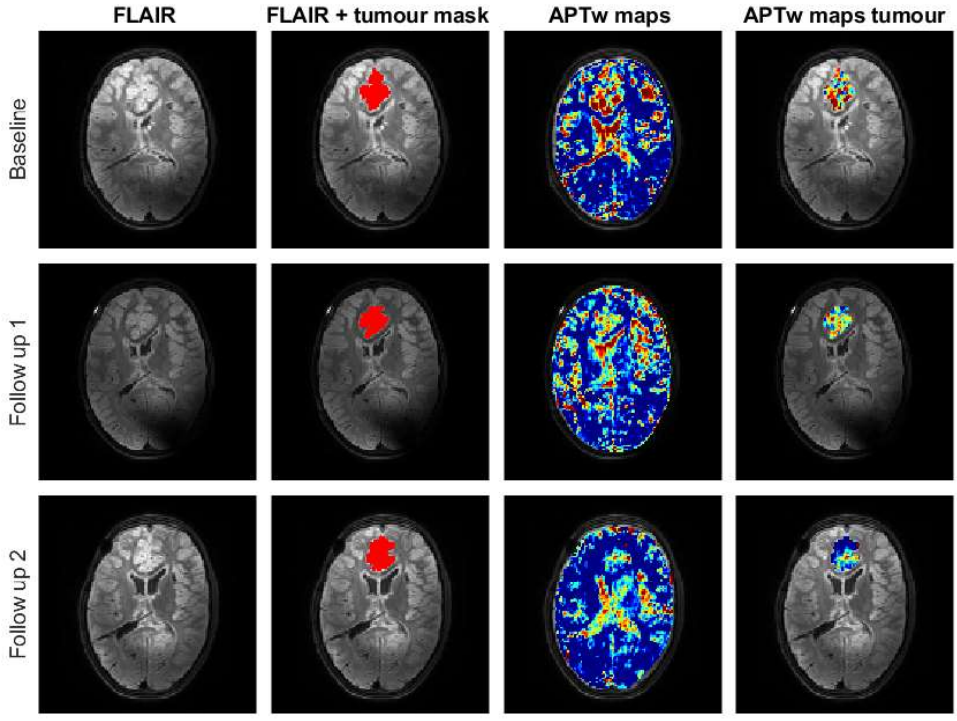

Figure G.5: Example of APTw maps quantified with MTRasym of patient 5.

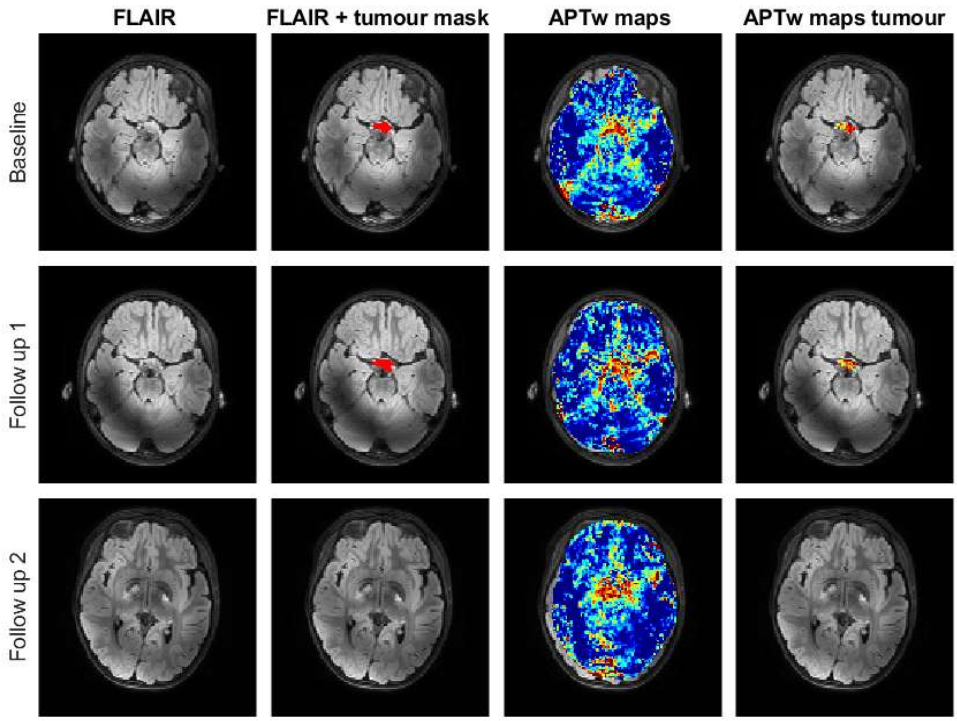

Figure G.6: Example of APTw maps quantified with MTRasym of patient 6.

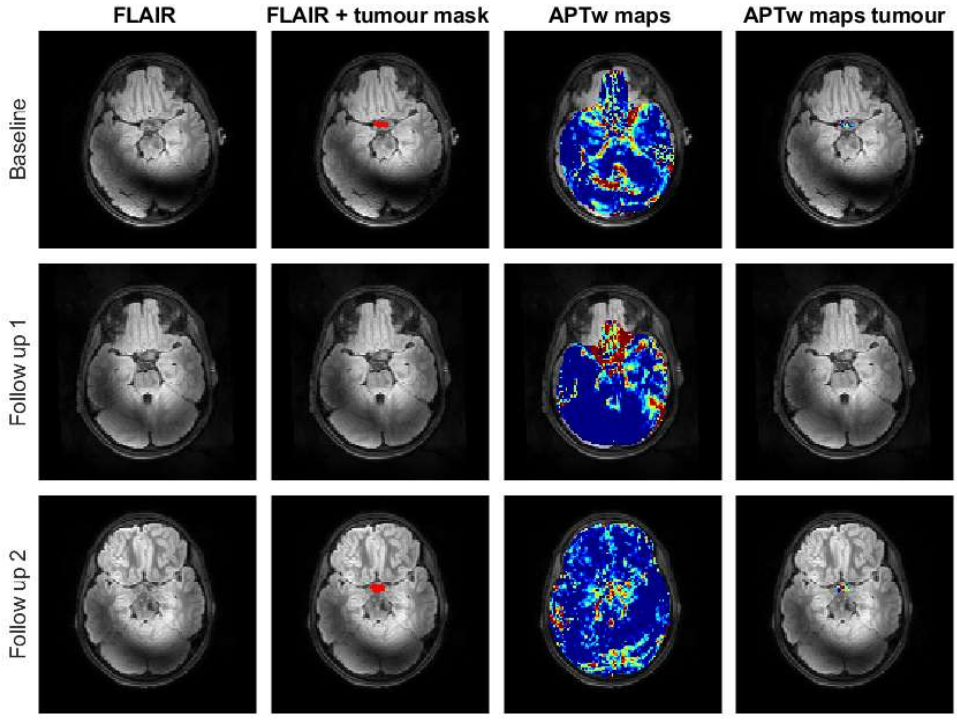

Figure G.7: Example of APTw maps quantified with MTRasym of patient 7.

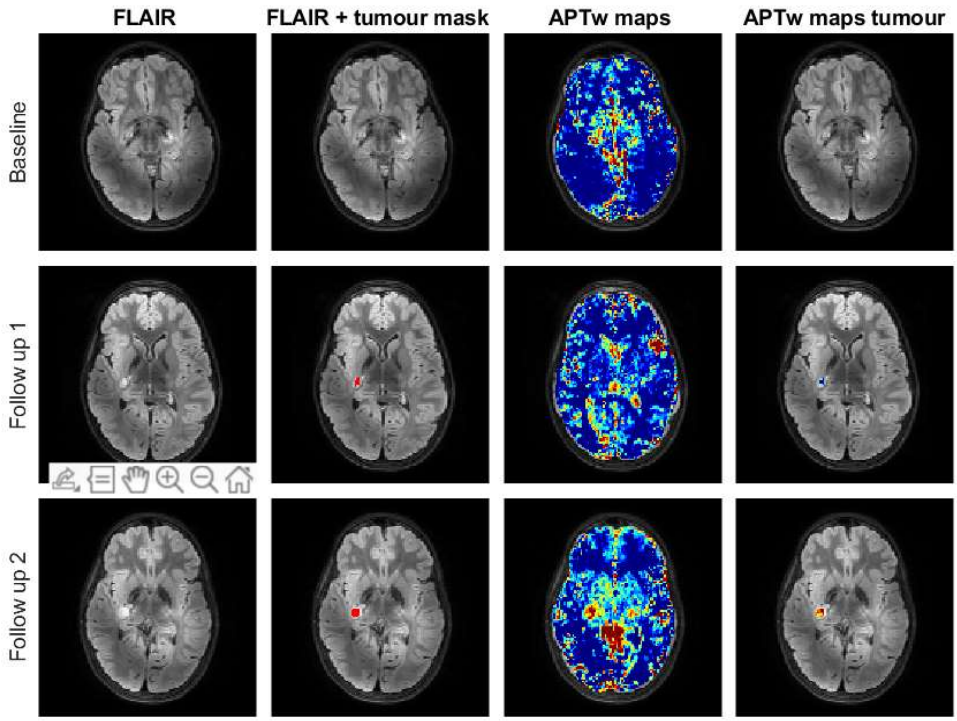

Figure G.8: Example of APTw maps quantified with MTRasym of patient 8.

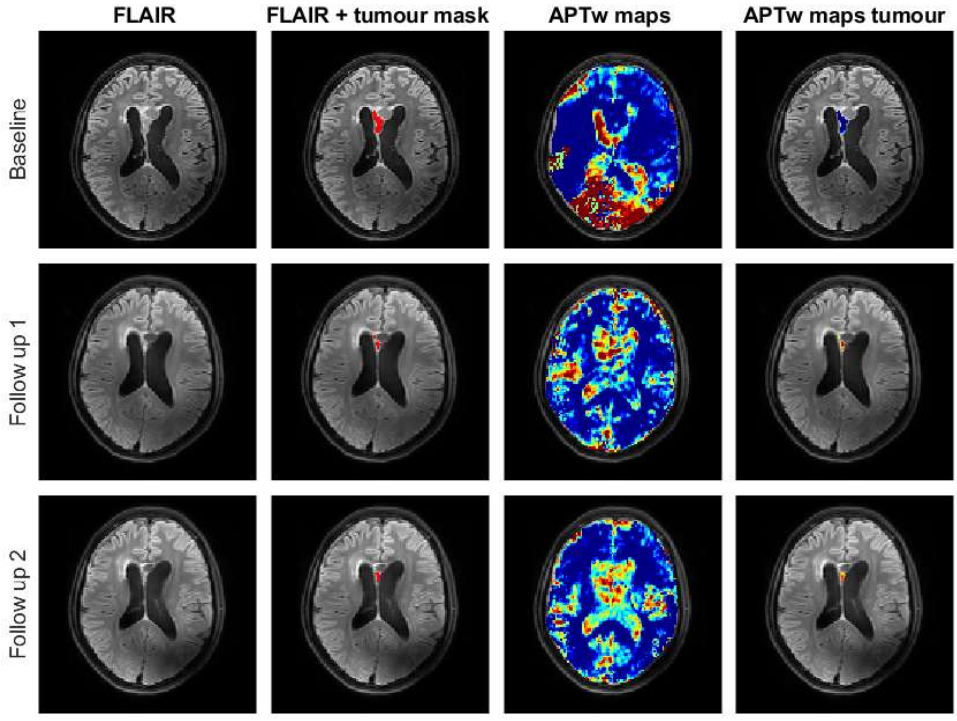

Figure G.9: Example of APTw maps quantified with MTRasym of patient 9.

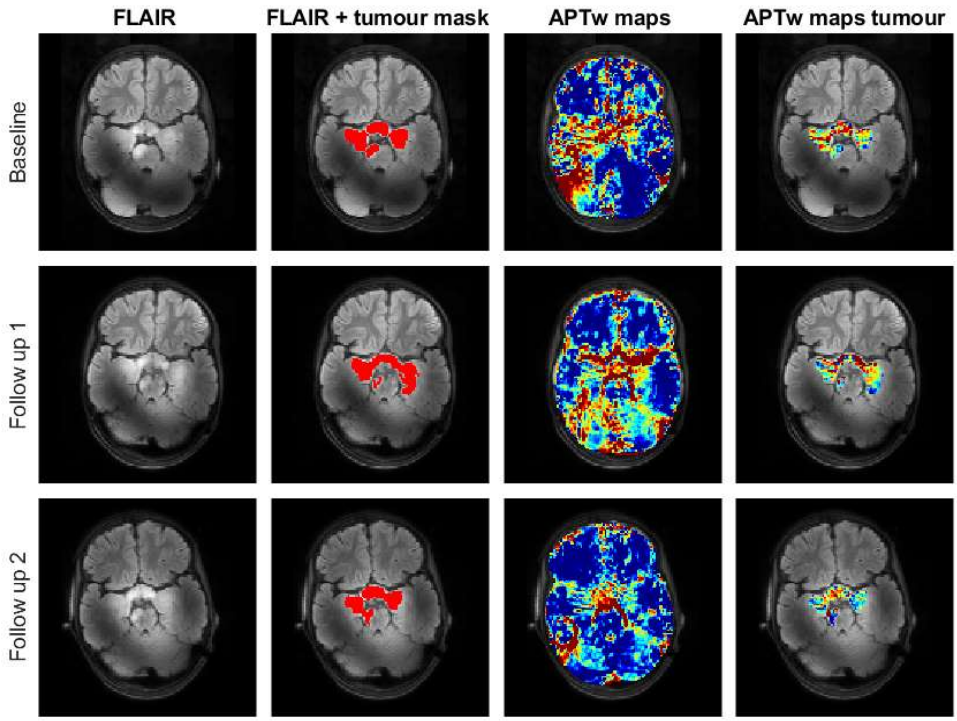

Figure G.10: Example of APTw maps quantified with MTRasym of patient 10.

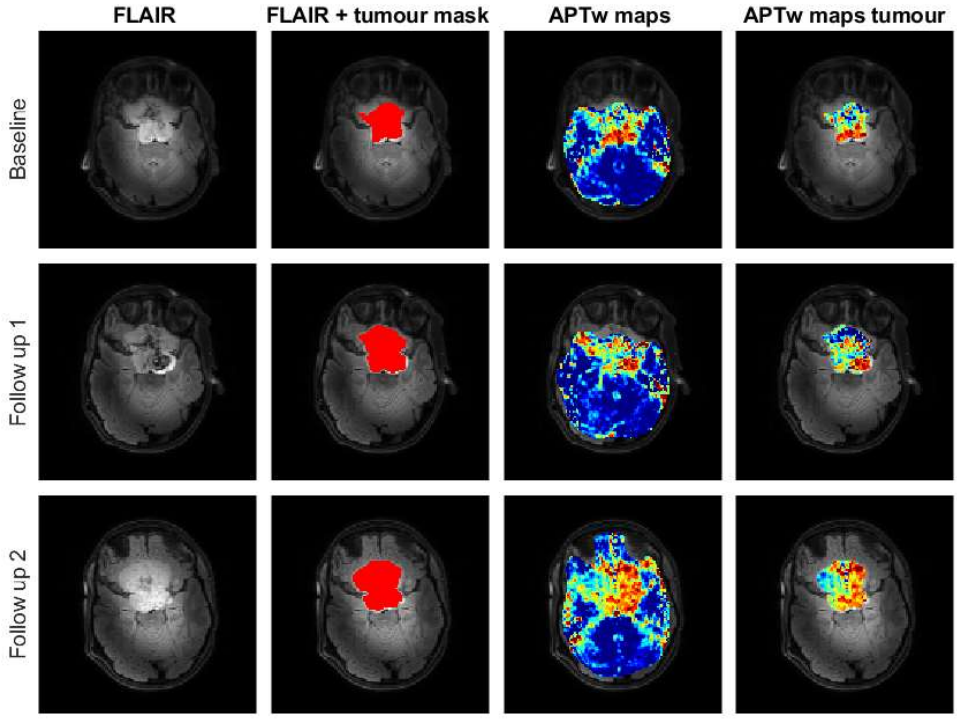

Figure G.11: Example of APTw maps quantified with MTRasym of patient 11.

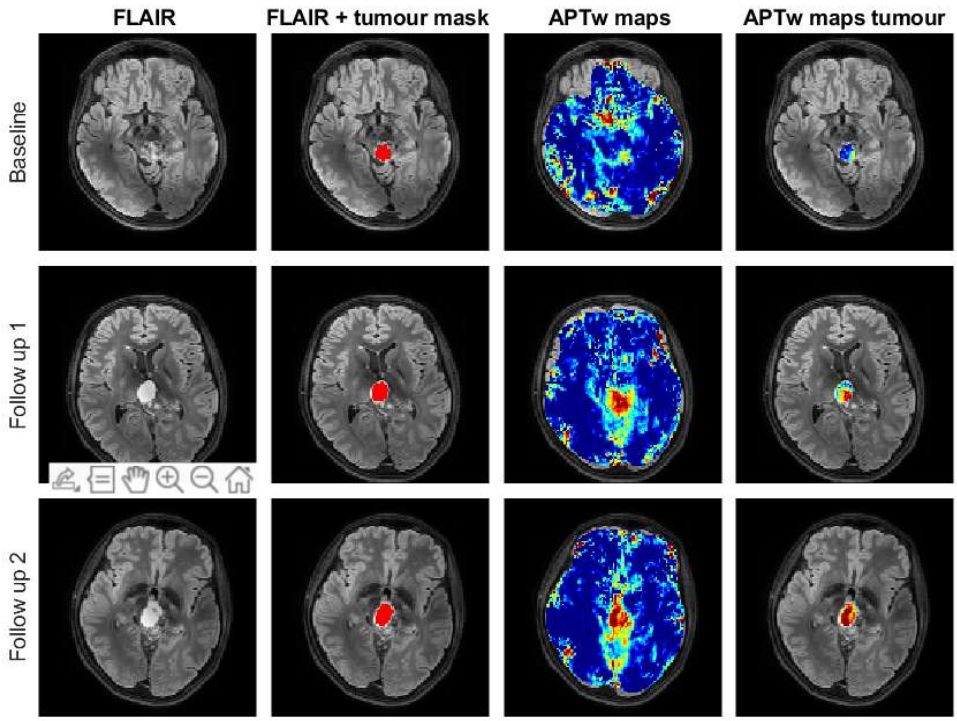

Figure G.12: Example of APTw maps quantified with MTRasym of patient 12.

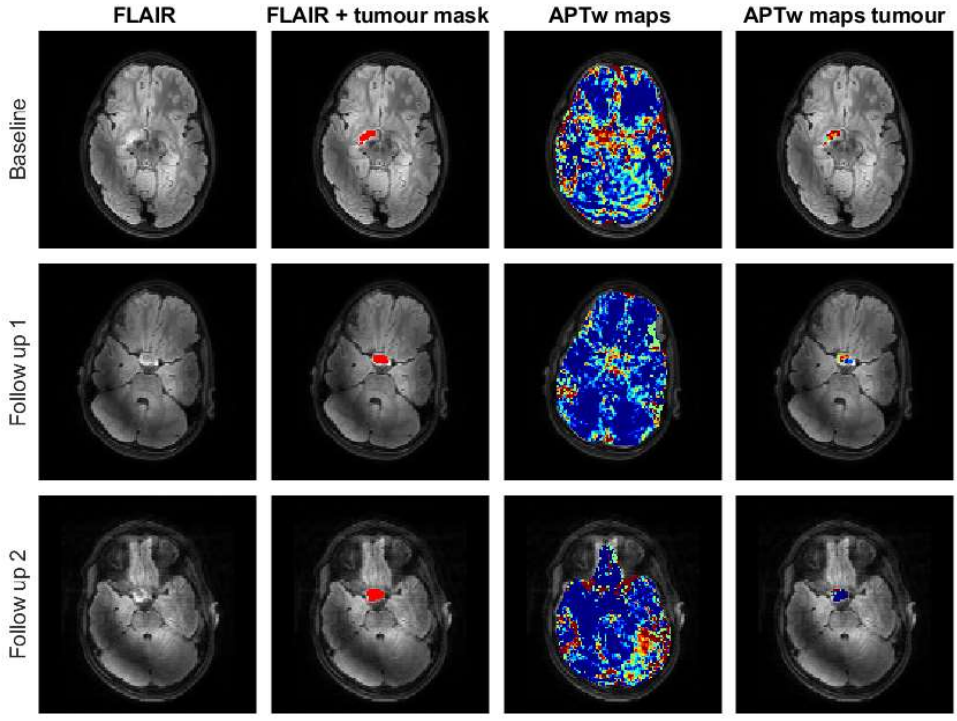

Figure G.13: Example of APTw maps quantified with MTRasym of patient 13.